A comparison of MODTRAN and RTTOV radiative transfer models for lake surface water temperature retrieval

Master's Thesis

Faculty of Science

University of Bern

presented by

Sebastian Schulze

2012

Supervisor:

Dr. Stefan Wunderle

Institute of Geography and Oeschger Centre for Climate Change Research

Advisor:

Dr. Michael Riffler

Institute of Geography and Oeschger Centre for Climate Change Research

To my parents Ralph & Birgit

Acknowledgements

I would like to thank all the people who contributed to the realization of this work and who supported my throughout the course of my studies.

In particular, I would like to express my gratitude to my supervisor Dr. Stefan Wunderle and my advisor Dr. Michael Riffler for giving me the opportunity to writing a Master's thesis in the Remote Sensing Research Group, while taking my personal interests into consideration. Their patience and critical input built the fundament for the success of this work. Dr. Michael Riffler's deserves a special acknowledgement for answering the plethora of my technical questions and for contributing a sizable amount of know-how to the completion of this project in time. In addition I would like to thank Dr. Fabia Hüsler for her kind advices and encouragements, as well as Christoph Neuhaus for his technical support in urgent matters and regardless of the daytime they occurred.

A very special thanks goes to Stefan Muthers. Stefan's support during the year since I have known him is hard to put into a single sentence. His contributions include roles as friend, advisor, editor and listener, and all of them inherit his stoic patience and genuine modesty. Another thankyou goes to my dear friends Christian, Marco, Moritz, Philip and Stephan, who did a diligent job on editing parts of this thesis in their free time. Finally, I would like to thank my girlfriend Fabienne for her patience and understanding during the last two years.

Before all others, I would like to thank my family for their unconditional love and support throughout all these years.

Abstract

Lake ecosystems and their catchments are known to correspond to climatic change in a complex manner and with implications for humans, animals and plants. Lake water temperature can constitute a key variable for investigations on the cause and impacts of climate variability on regional scales. Remote sensing studies on long-time series satellite observations have revealed and confirmed the viability of these data archives for spatially covering water surface temperature measurements with the split-window technique. The split-window technique utilizes the proportional relationship of the wave-length dependent atmospheric attenuation and the measured radiance difference in two nearby wavebands, typically in the atmospheric window around 8 – 13 μm. A multi-linear regression from simulated brightness temperatures is able to deliver a set of regression coefficients, which can be used for retrieving accurate estimations of lake surface water temperatures from satellite observations.

In this study the split-window method proposed by Hulley et al. (2011) is used in order to retrieve lake water surface temperatures (LSWT) from satellite observations of the NOAA AVHRR sensor series for six large Swiss lakes. Atmospheric profiles of the European Center for Medium-Range Weather Forecasts (ECMWF) are employed in combination with the Moderate Resolution Transmittance (MODTRAN) radiative transfer code in order to derive the split-window coefficients. Finally, the accuracy of this model is evaluated against the institute's operational LSWT model that implements the Radiative Transfer for TIROS (Television Infrared Observation Satellite) Operational Vertical Sounder (RTTOV) code with the help of in situ water temperature measurements as validation sources. In this context, the study faces three main objectives: (i) developing a routine that performs radiative transfer simulations with the radiative transfer model MODTRAN, (ii) deriving lake surface water temperatures with the split-window technique and (iii) comparing the MODTRAN computed LSWTs to LSWTs derived from the radiative transfer model RTTOV as well as to the in situ water temperature archive. The investigation is based on NOAA 17 and NOAA 18 AVHRR observations from 2003 to 2010, which were obtained from the data archive of

the Remote Sensing Group of the University of Bern. The comparison of the simulated LSWTs is carried out on three selected in situ data sets of Lake Constance and Lake Geneva from a larger in situ data archive, which was collected from several Swiss, French and Austrian administration offices and scientific institutions in the framework of this study. The model performance was evaluated in terms of the accuracy against locally measured water temperatures and compared to the accuracy of a reference algorithm that implements the RTTOV radiative transfer model.

The results indicate a good performance of the RTTOV algorithm and the MODTRAN algorithm, with slightly smaller satellite-averaged root mean square errors (~0.01 K) and biases (~0.07 K) for the RTTOV model. A comparison of the raw simulated brightness temperature outputs for AVHRR channels 4 and 5 indicated a growing divergence for large viewing zenith angles above 40° and a general dependency of at least one of the models on this parameter. This divergence could however not been detected in the final LSWTs anymore. An investigation of the simulated LSWT sensitivities against wind speed, viewing angle and maximal relative humidity showed relative invariances for both models. A spatial comparison of LSWTs for Lake Geneva and Lake Constance supported the hypothesis that MODTRAN and RTTOV perform similarly with spatial standard deviations in the between 0.006 K and 0.02 K for two selected scenes in April, 2007. Considering these results as well as additional economic and performance criteria the decision for implementing RTTOV instead of MODTRAN into the operationally working LSWT retrieval algorithm at the Institute could be justified and reasoned. With the approach and the parameters sets used in this study MODTRAN did not show superior performance over RTTOV for lake surface water temperature assessment from NOAA17 and NOAA18 AVHRR satellite data.

Contents

List of figures

List of tables

Abbreviations

a.s.l.	-	Above sea level
AATSR	-	Advanced Along Track Satellite Radiometer
ASCII	-	American Standard Code for Information Interchange
AVHRR	-	Advanced Very High Resolution Radiometer
BDS	-	Lake Constance
Brgz	-	In situ temperature station maintained the by the Amt der Vorarlberger Landesregierung located in Bregenz, Austria
BT	-	brightness temperature
BT4	-	Brightness temperature at AVHRR channel 4
BT45	-	Brightness temperature difference of AVHRR channel 4 minus channel 5
BT5	-	Brightness temperature at AVHRR channel 5
BTD4	-	RTTOV minus MODTRAN brightness temperature difference for AVHRR channel 4
BTD45	-	RTTOV minus MODTRAN brightness temperature difference for AVHRR channel 4 minus channel 5
BTD5	-	RTTOV minus MODTRAN brightness temperature difference for AVHRR channel 5
ECMWF	-	European Center for Medium-Range Weather Forecasts
ECV	-	Essential Climate Variable
EM	-	Electromagnetic
Eumetsat	-	European Organisation for the Exploitation of Meteorological Satellites
GCOS	-	Global Climate Observing System
GFS	-	Lake Geneva

GIUB	-	Geographical Institute of the University of Bern
HITRAN	-	High-resolution Transmission molecular absorption database
INRA	-	In situ temperature station maintained by the Institut national de la recherche agronomique located in Lake Geneva
IPCC	-	Interngovernmental Panel of Climate Change
IR	-	Infrared spectral range
LGS	-	Lake Lugano
LSWT	-	Lake surface water temperatures
MetOp	-	Meteorological Operational satellite
MODTRAN	-	Moderate Resolution Transmittance
NASA	-	National Aeronautics and Space Administration
NBS	-	Lake Neuchâtel
NIR	-	Near infrared spectral range
NOAA	-	National Oceanic and Atmospheric Administration
Nxx	-	Satellite platform xx of the NOAA-series, xx={17, 18}
RSGB	-	Remote Sensing Group Bern
RT	-	Radiative transfer
RTTOV	-	Radiative Transfer for TIROS (Television Infrared Observation Satellite) Operational Vertical Sounder
SESR	-	Surface-emitted surface-reflected
SST	-	Sea-surface temperature
TIR	-	thermal infrared spectral range
UniK	-	In situ temperature station maintained by the University of Constance
VIS	-	Visible spectral range
VWS	-	Lake Lucerne
ZUE	-	Lake Zurich

Chapter 1

Introduction

The unique role of terrestrial water in the climate system has been the focus of extensive research (Intergovernmental Panel on Climate Change (IPCC), 1990, 1995, 2001, 2007). Due to its physical properties (e.g. high specific heat capacity, high heat of vaporization) small changes in the water temperature might yield distinctive feedback effects to the interaction between the cryosphere, hydrosphere and atmosphere (cf. Bindoff et al., 2007). Accurate water surface temperature retrieval is of crucial importance for the understanding and precise prediction of the dynamics of energy fluxes in the climate system and to addressing the raising issues related with climate change (Bindoff et al., 2007). Among others, these issues involve tasks of seasonal weather and ocean forecasting, ecosystem assessment, industrial fishing and tourism research (Castro et al., 2010; Donlon et al., 2007; and Walton et al., 1998, for further applications and references). In the framework of the Global Climate Observing System (GCOS) sea- and lake surface water temperatures were defined as two of 50 Essential Climate Variables (ECV) and were included into the long-term monitoring program for assessing the state of the climate system (GCOS, 2006). Hence, it is not surprising that the research community involved in water surface temperature retrieval is well organized and eager to improve the retrieval techniques, e.g. the Group for High Resolution Sea Surface Temperature (GHRSST) (cf. Donlon et al., 2007; Kaiser-Weiss et al., 2011).

Limnological studies revealed and confirmed the capability of large inland water body temperatures to serve as indicators of climate change (e.g. Austin & Colman, 2007; Livingstone, 2003; Straile et al., 2010). While lakes are known to exhibit sensitive responses to climate in general (Rosenzweig et

al. 2007), the individual impacts of climate change on lakes tend to vary distinctively with geographic location, elevation, morphometry, regional climate, vegetation in the catchment and the land use (Adrian et al., 2010). Responses can include direct impacts on the chemical, physical and biological properties of the lakes' ecosystems as well as delayed feedback mechanisms (Adrian et al., 2010). Consequences for Swiss lakes, for example, can range from changes in the thermal structure, over shifts from cold-water to warm-water fish species, to earlier onsets of algae blooms, and less frequent and extended lake-ice coverage (OcCC, 2007 and sources therein). Adrian et al. (2010) collected and reviewed key response variables to climate change that have been used throughout numerous studies in order to measuring the impact of climate change on lakes. They identified seven indicators for key lake properties: (1) water temperature, (2) water level, (3) ice phenology, (4) chemical variables, (5) dissolved organic carbon (DOC), (6) oxygen concentrations and (7) lake biota. Particularly, water temperatures of upper lake levels, termed epilimnion, revealed a high correlation with regional air-temperatures trends in North America (Coats et al., 2006; Schneider et al., 2009), Europe (Livingstone & Lotter, 1998; Peeters et al., 2002), Asia (Hampton et al., 2008) and Africa (O'Reilly et al., 2003; Tierney et al., 2010; Verburg & Hecky, 2009). Additionally, Adrian et al. (2010) reviewed a series of direct and indirect influences of lake water temperature to other key response variables, which makes the rather easily accessible water temperatures a prominent indicator for alterations in the lake ecosystem.

Globe-covering satellite observations are well-known to constitute a powerful instrument for elucidating climate trends from the most recent decades on various scales (GCOS, 2006). Satellite images deliver valuable spatial data sets of lake surface temperatures (e.g. Oesch et al., 2008; Schneider & Hook, 2010; Schneider et al., 2009) or of lake-ice phenology (e.g. Latifovic & Pouliot, 2007). Especially thermal infrared studies revealed their potential for monitoring lake surface water temperatures (LSWT) in distinct areas of the globe (e.g. Hulley et al., 2011; Oesch et al., 2005; Wooster et al., 2001). The split-window approach represents a robust and effective procedure for water surface temperature retrieval and is used for the operational water surface temperature products of the Moderate Resolution Imaging Spectroradiometer (MODIS; Brown & Minnett, 1999), the Advanced Along Track Scanning Radiometer (AATSR; MacCallum & Merchant, 2011) and the Advanced Very High Resolution Radiometer (AVHRR; Kilpatrick et al., 2001). The split-window technique utilizes two nearby channels in the thermal infrared (TIR) bands within an atmospheric window, which can be modeled with radiative transfer simulations, corresponding atmospheric profiles and known surface emissivity (Hulley et al., 2011). A subsequent multi-linear regression of the simulated data against either modeled (Závody et al., 1995) or coincidently locally measured

(Kilpatrick et al., 2001) water-surface temperatures yields the split-window coefficients for derivations of satellite observed water-surface temperatures.

Water surface temperature measurements are traditionally performed with ground-based or space-borne sensors (Donlon et al., 2002a, 2007; Kilpatrick et al., 2001). While ground-based measurements with calibrated instruments mounted on ships, buoys and research stations are known to deliver very accurate results, their availability is constrained in time and space (Donlon et al., 2002a). Thermal infrared remote sensing from space has recently proven its capability to close this spatio-temporal gap, with tenable constraints on absolute accuracy (e.g. Castro et al., 2010; Gentemann, 2003; Hook et al., 2003, 2004). A promising long time series for investigations on regional to global scales has been acquired from the AVHRR on the United States National Oceanic and Atmospheric Administration (NOAA) platforms and the Meteorological Operational Satellites (MetOp) on the European Organisation for the Exploitation of Meteorological Satellites (Eumetsat) platforms. The AVHRR has been operating and recording data from the Earth's surface continuously in three and later on four infrared (IR) channels since 1981 (Casey et al., 2010; Walton et al., 1998). Exploiting this time series the Remote Sensing Research Group of the University of Bern, Switzerland (RSGB) has launched a project to deriving lake surface water temperatures for Swiss lakes from 1989 until today. The project is part of the Global Climate Observing System and funded by MeteoSchweiz, Switzerland.

The RSGB adopted an algorithm proposed by Hulley et al. (2011) in order to retrieve LSWTs for Swiss lakes from the satellite archive (Michael Riffler, results not published yet). This algorithm is based on an inland water body split-window formulation, which utilizes regional atmospheric profiles for radiative transfer simulations in order to derive a set of regression coefficients for a direct computation of LSWTs from satellite data. Hulley and his co-workers investigated the performance of their regional model in comparison with the global conditions optimized standard products of the Moderate Resolution Imaging Spectroradiometer (MODIS) and the Along Track Scanning Radiometer (AASTR), and when applied to two large fresh-water lakes in the western USA. For their model, they found root mean square errors (RMSE) approximately 0.35 K smaller than the operational products of MODIS and AASTR. Based on the accurate results of Hulley et al (2011) the RSGB decided to implement their concept with the Radiative Transfer for TIROS (Television Infrared Observation Satellite) Operational Vertical Sounder (RTTOV) radiative transfer code in combination with regional temperature and relative humidity profiles obtained from the European Center for medium-range weather forecasts (ECMWF) for the operational Swiss LSWT product (results not published yet).

The current study is designed to investigate the performance of the operational RTTOV-based algorithm by means of a second radiative transfer based algorithm. This algorithm was implemented in the course of this study and is capable of performing radiative transfer simulations for a predefined period and set of target pixels, of computing split-window coefficients for these target pixels and of calculating LSWTs. In this context, the Moderate Resolution Atmospheric Transmission (MODTRAN) model has been implemented based on the approach of Hulley et al. (2011). The algorithm is optimized for lake-surface elevation and local atmospheric as well as surface temperatures conditions of the assigned target pixels. Since the RTTOV model has been optimized for fast computation, it can be expected that the elaborated MODTRAN model might deliver smaller overall errors in exchange for a prolonged period of computation. The model comparison is carried out on three in situ water temperature data sets from Lake Constance and Lake Geneva with a fine temporal resolution for robust statistical inferences. The co-variables wind speed, viewing zenith angle and maximum relative humidity are investigated for their influence on the accuracy of both models. The performance statistics from the abovementioned investigations is finally being used to formulate an evaluation of the suitability of the RTTOV model and the MODTRAN model for LSWT computations of Swiss lakes. Summarizing, this study faces three main objectives: (i) to develop a routine that performs radiative transfer simulations with MODTRAN, (ii) to derive lake surface water temperatures with the split-window technique and (iii) comparing the MODTRAN computed LSWTs to LSWTs derived from the radiative transfer model RTTOV as well as to the in situ water temperature archive.

Chapter 2

Theory of LSWT retrieval

Chapter 2 covers the physical methods that are necessary to derive accurate LSWTs from satellite data. In the first part the text will briefly guide through the fundamental physical concepts underlying thermal infrared (TIR) remote sensing and radiative transfer simulations. The second part explains the emissivity model that is used for computing water surface emissivity. The third and last section gives a brief overview of the methods utilized in most operational LSWT retrieval algorithms with a strong focus on the split-window technique, which concomitantly represents the technique of choice for LSWT retrieval in the present study.

2.1 Basics of thermal infrared remote sensing and radiative transfer modeling

Understanding the transfer of electromagnetic radiation in the atmosphere is of crucial importance to remote sensing. Atmospheric transfer processes involve multiple scattering and absorption by atmospheric constituents such as gases and particulate matter (Wendisch & Yang, 2012). The methodological framework to describe radiative transfer in detail consists of sophisticated methods from mathematics and physics (see Liang, 2004; Petty, 2006; Wendisch & Yang, 2012 for comprehensive overviews). A comprehensive review of those methods lies far beyond the scope of this study. However, the following section is arranged to summarize the basic concepts, which are

involved in TIR remote sensing of terrestrial surfaces from space and briefly reviews the underlying principles of radiative transfer in a very general way.

2.1.1 The fundamental laws of radiative transfer

The following section introduces the basic principles that are exploited in radiative transfer and thermal infrared remote sensing. Thereby this section draws fundamentally on chapters 6 and 8 of Petty (2006).

The classical principles of radiative transfer, and thus of any remote sensing technique, were developed by only a handful of scientists in the second half of the 20th century. These principles characterize the impact of electromagnetic radiation on particle matter, thereby obeying the laws of thermodynamics. As formulated in Kirchhoff's law, in thermal equilibrium and for a given wavelength λ and viewing angle ϕ, the amount of radiation emitted by an object is equal to the amount of radiation absorbed

$$\varepsilon(\lambda, \phi) = \alpha(\lambda, \phi) \tag{2.1}$$

, where $\varepsilon(\lambda,\phi)$ is the object's emissivity and $\alpha(\lambda,\phi)$ its absorptivity. An object with a temperature T will emit radiation with an intensity $B_\lambda(T)$ [$W \cdot m^{-2} \cdot \mu m^{-1} \cdot sr^{-1}$] according to Planck's function

$$B_\lambda(T)d\lambda = \frac{2hc^2}{\lambda^5\left(e^{\frac{hc}{\lambda kT}-1}\right)}d\lambda \tag{2.2}$$

, with Planck's constant h = $6.626 \cdot 10^{-34}$ J·s, the speed of light c = $2.998 \cdot 10^{8}$ $m \cdot s^{-1}$ and the Boltzmann's constant k = $1.381 \cdot 10^{-23}$ $J \cdot K^{-1}$. The peak of Planck's function at a wavelength λ_{max} is inversely proportional to the object's temperature T. This relationship is described by Wien's displacement law

$$\lambda_{max} \cdot T = k_W \tag{2.3}$$

, where k_W = 2897 μm·K denotes Wien's displacements constant. If an object absorbs radiation perfectly – and according to Kirchhoff's law emits perfectly – it is called blackbody. An object which does not perfectly absorb radiation is often referred to as a greybody. While Planck's function allows to compute the monochromatic intensity of a blackbody, integration of the Planck's function over the

entire electromagnetic spectrum and the entire hemisphere equals the broadband flux F_B of a blackbody

$$F_B = \sigma \cdot T^4 \tag{2.4}$$

, where $\sigma \approx 5.67 \cdot 10^{-8}$ $W \cdot m^{-2} \cdot K^{-4}$. This proportional relationship of the blackbody broadband flux to the fourth power of its temperature T is referred to as the Stefan-Boltzmann law.

Keeping these rather idealistic but fundamental principles of radiative transfer in mind, one can account for the concepts of emissivity, the derivation of the brightness temperature, the Beer-Bourguer-Lambert law and Schwarzschild's equation. These principles form the basis for interpreting satellite observations from space. Figuratively, the emissivity concept apprehends the deviation in emissivity of a greybody object from the same object treated as a blackbody (Petty, 2006). In this way, emissivity in-between two wavelengths λ_1 and λ_2 can be calculated with a simplified ratio of the actually observed broadband flux $F(\lambda_1, \lambda_2)$ to the virtually idealized blackbody flux $F_B(\lambda_1, \lambda_2)$ from the same object.

$$\varepsilon = \left[\frac{\varepsilon_{graybody}}{\varepsilon_{blackbody}}\right] = \frac{F(\lambda_1 \lambda_2)}{F_B(\lambda_1 \lambda_2)} \tag{2.5}$$

As stated above Planck's function directly relates the temperature of a blackbody with its emission intensity at a specific wavelength. The inverse relationship is exploited in thermal infrared remote sensing during brightness temperature derivation

$$T_B = B_\lambda^{-1}(I_\lambda) \tag{2.6}$$

, where B_λ^{-1} is the inverse of the Planck function, and I_λ the actually measured intensity for a given wavelength. Most land and water surfaces as well as dense cloud layers are almost blackbodies in the thermal infrared spectrum of electromagnetic radiation (TIR), having emissivities ε close to 1. Hence, their brightness temperature T_B can reliably be approximated with their physical temperature when observed through a transparent atmosphere (Petty, 2006). The atmosphere appears relatively transparent in regions of the electromagnetic spectrum, where none of the abundant atmospheric constituents possesses an intrinsic absorption feature. These regions are most widely referred to as spectral or atmospheric windows. An important spectral window for thermal infrared remote sensing lies in the vicinity of 11μm, which explains why the majority of operational weather satellites contains at least one channel that acquires spectral data within this region. Regarding many applications in remote sensing, meaningful observation of the Earth's surface will only be feasible within these spectral windows. Nonetheless, by multiple scattering and absorption the atmospheric

constituents make their contribution to the total radiation acquired at the sensor. Beer's law allows to quantify the reduction in radiant intensity for radiation propagating through a homogenous, finite layer between two points s_1 and s_2 with a constant extinction coefficient β_e

$$I_\lambda(s_2) = I_\lambda(s_1) \cdot exp\left[-\int_{s_1}^{s_2} \beta_e(s)\, ds\right] \quad , \forall s_2 \geq s_1 \tag{2.7}$$

, where $I_\lambda(s_1)$ is the initial radiant intensity when entering the layer at s_1, $I_\lambda(s_2)$ denotes the radiant intensity after propagation of the layer, and the exponential term $exp\left[-\int_{s_1}^{s_2} \beta_e(s)\, ds\right]$ is the transmittance (or transmissivity) t of a finite path. The integral $\int_{s_1}^{s_2} \beta_e(s)\, ds$ can be referred to as the opacity[1] τ of the finite path.

Now, as the radiant extinction by the atmospheric constituents can be quantified for a given homogeneous atmospheric path, Schwarzschild's equation allows decoupling of the intensities contributed by the atmosphere and by the surface for any given wavelength

$$I(\tau = 0) = I(\tau) \cdot e^{-\tau} + \int_0^{\tau} B e^{-\tau'}\, d\tau' \tag{2.8}$$

, where $I(\tau = 0)$ means the radiant intensity measured at the sensor, the first term on the right hand side $I(\tau) \cdot e^{-\tau}$ represents the emission reduction by attenuation along the atmospheric path of sight, while the integral refers to the additional contribution of each homogenous atmospheric layer to the net emission observed. An important assumption exploited by Schwarzschild's equation refers to the possibility of separating the entire optical path from the surface to the sensor into individual homogenous sub-paths, whose sum yields the total optical path again (Petty, 2006). Petty (2006) denotes Schwarzschild's equation "[…] as the most fundamental description of radiative transfer in a nonscattering medium" [p. 205]. This equation enables calculations of diffusive radiation in a plane-parallel, horizontally homogeneous atmosphere and in fact, it constitutes the starting point for every algorithm involving observations of surface water temperatures from space, although it might not be mentioned every single time.

[1] Other widely used terms for opacity are optical path, optical thickness or optical depth.

2.1.2 Radiative transfer modeling in thermal IR satellite remote sensing

Section 2.1.2 is designed to sketch the idea of modeling radiation transport trough the atmosphere in the thermal infrared spectrum of electromagnetic radiation. In this context the Earth's longwave net radiation ΔF can be quantified as the difference between the downward Flux $F_{\downarrow}$ and the upwelling Flux $F_{\uparrow}$.

$$\Delta F = F_{\downarrow} - F_{\uparrow} \tag{2.9}$$

The longwave downward flux $F_{\downarrow}$ quantifies the radiation (re-)emitted from the atmosphere. However, surface temperature retrieval from space is primarily based on a characterization of the temperature dependent upwelling flux, the surface broadband emissivity and the transmissivity of the atmosphere (Liang, 2004).

Remember that Schwarzschild's equation makes it possible to quantify the radiant intensity in a plane-parallel and horizontally homogeneous layer and that radiant flux is nothing else than the integration over the intensity contributions from all possible incident directions. Separation of the atmosphere into several plane-parallel and horizontally homogeneous layers and subsequent integration over all layers then allows quantification of radiation transfer for the entire atmosphere. For a satellite sensor above the top of atmosphere and viewing downward toward an idealized blackbody surface, it is convenient to consider a slightly transformed Scharzschild's equation (2.8)

$$I_{\uparrow}(z = \infty) = B(T_S) \cdot e^{-\tau} + \int_0^{\infty} B(z) \cdot e^{-\tau'} dz \tag{2.10}$$

, where $I_{\uparrow}(z = \infty)$ specifies any point beyond the top of the atmosphere, $B(T_S)$ is the Planck function for the surface temperature T_S attenuated by the transmittance $e^{-\tau}$ along the path from the surface to the top of the atmosphere, and the integral is a weighted sum of the individual attenuation contributions $e^{-\tau'}$ of each finite atmospheric layer z (Petty, 2006). The surface term depends on the nature of the surface (i.e. its emissivity) as well as on the upward reflection of incident radiation from the surface. In the course of this study, the water surface is treated as a Lambertian reflector throughout the thesis, which means that radiation is reflected isotropically into space. Notice however, that surface reflection beyond 4 μm is becoming negligible compared to the radiant emission of the Earth (Petty, 2006). How surface emissivity is treated during the radiative transfer simulations is extensively described in section 2.2. The second, atmospheric term of equation 2.10 depends on the extinction of radiation within each individual layer at height z. As atmospheric scattering greatly depends on the particle size, scattering in the TIR can safely be neglected, when

precipitation (e.g. droplets, ice crystals, particulate matter) within the observation period can be excluded (Petty, 2006). Since only "clear sky" satellite observations are considered throughout the entire study, scattering in the TIR wavelengths by atmospheric constituents will not be considered. The absence of scattering also simplifies the angular dependence of radiance significantly, which now only depends on the viewing zenith angle and is assumed to be isotropic in azimuthal direction (Liang, 2004).

With equation 2.10, one can compute the upwelling monochromatic intensity $I_{\uparrow}$ for any given wavelength. For any given waveband however, a spectral integration over a range of wavelengths is needed. This integration has to incorporate the individual absorption features of all atmospheric constituents in the respective waveband. Classical techniques range from very accurate but computer intensive line-by-line methods, over less accurate but computationally more efficient band models, to statistical techniques such as the correlated k-distribution method, which presents a good trade-off between accuracy and efficiency (Liang, 2004). Details concerning these and other sophisticated statistical methods can be reviewed in Liang (2004) and Wendisch & Yang (2012). The current version of MODTRAN uses the correlated k-distribution method, which determines the wavelength-dependent absorption coefficient over a probability density function (Kneizys et al., 1996).

Radiative transfer models are made to numerically evaluate the radiation budget (e.g. heating and cooling) at each particular layer, when properly related to profiles of temperature, humidity and trance gas compositions (Petty, 2006). Simulations are typically run with either measured atmospheric profiles or with idealized profiles, called model atmospheres. Model atmospheres can be provided for several climatic large-scale regimes and most distinctively vary in their temperature and water vapor profiles. In the context of this study, MODTRAN's standard atmospheres for mid-latitude summer and winter profiles have been synchronized with atmospheric profiles from reanalysis data (see chapters 3 and 4 for further details). In a final step the radiance output is weighted and integrated for the specific response of the sensor in order to obtain band-specific averaged radiances. Berk (2006) describes an analytic approach for the convolution of spectral band average radiances into sensor-specific brightness temperatures, as it is provided with the most recent versions of the MODTRAN band model.

2.2 Emissivity of large natural water surfaces in the 8 - 13 μm atmospheric window

Water surface emissivity is one crucial parameter for temperature retrieval with the split-window technique (Masuda, 2006), although water surface emissivity is known to be typically high and spectrally flat (Hulley et al., 2011). In order to meet current accuracy requirements for LSWT retrieval of ± 0.2 °C (GCOS, 2006) accurate water surface emissivity modeling has been a subject of extensive research (e.g. Friedman, 1969; Masuda, 2006; Masuda et al., 1988; Wu & Smith, 1997).

The following review of landmark studies on water-surface emissivity modeling is arranged to give a brief introduction into the topic. Cox and Munk (1954) took aerial photographs of sun glitter and developed a statistical slope characterization of the wind-roughened sea surface. Saunders (1968) used the slope statistics of Cox and Munk to compute a viewing angle dependent rough sea surface reflectivity, while accounting for effects of wave shadowing, multiple surface reflections and anisotropic irradiance. On the basis of the model developed by Takashima & Takayama (1981), Masuda et al. (1988) improved the sea surface emissivity modeling by including the wavelength dependent variations of the refractive index of sea water derived by Hale and Querry (1973) with salinity adjustments of Friedman (1969). Watts et al. (1996), and Wu and Smith (1997) used the direct emission as a radiation source to obtain the first order surface-emitted surface-reflected (SESR) emissivity. Recently, Masuda (2006) incorporated the second order SESR radiation into emissivity modeling in order to improve the computation at high emission angles, which was still underestimated in the precursory model of Masuda et al. (1988). In his model, Masuda (2006) utilizes a weighting function derived from the slope's probability distribution function in order to determine the probability for the source radiation to have been radiated from the sea.

A full derivation of the SESR emissivity is waived, because it is well documented in the publications of Masuda et al. (1988) and Masuda (2006). Non-specialists could additionally consider Takashima & Takayama (1981) as well as Wu and Smith (1997), who present a rather comprehensive derivation of the direct and SESR emissivity respectively, while more recent publications tend to presuppose knowledge about former models. The following paragraphs will only capture the key equations and ideas involved in the Masuda (2006) model.

For greybody surfaces, such as water in natural environments, the upwelling radiation $F_{\uparrow}$ is composed of a reflected and an emitted part (Saunders, 1967)

$$F_{\uparrow} = F_{refl} + F_{emit} \tag{2.11}$$

, where F_{refl} and F_{emit} denote the reflected and the emitted Flux, respectively. When the sea surface is roughened by wind-driven motion the observer receives emission from numerous small facets in the field of view (Wu & Smith, 1997). Consideration of the average emissivity of a wider sea surface over a longer period of time yields a mean emissivity $\bar{\varepsilon}$ that represents the integral effect of all contributing facets (Masuda et al., 1988). Following Cox and Munk (1954), the wind-depended facet slope distribution is Gaussian and isotrophic and can be expressed as

$$P(z_x, z_y) = (\pi\sigma^2)^{-1} \cdot exp\left[-\frac{(z_x^2 + z_y^2)}{\sigma^2}\right] \tag{2.12}$$

, where z_x and z_y are the slope components in orthogonal x- and y- direction with zero mean and root mean square of σ due to the isotropy assumption. While z_x and z_y are functions of the facet's geometry, σ is a function of wind speed. The equations are not provided here, but can be reviewed in Masuda et al. (1988), Masuda (2006) or Wu and Smith (1997). Following Cox and Munk (1954) and Saunders (1967, 1968), Masuda (2006) derived the mean sea surface emissivity $\bar{\varepsilon}(\vartheta)$ from a horizontal unit area of wind-roughened sea surface into direction ϑ as

$$\bar{\varepsilon}(\vartheta) = \frac{1}{cos\vartheta} \int_{-\infty}^{+\infty} \int_{-\infty}^{+\infty} \varepsilon(\chi) \cdot cos\chi \cdot sec\vartheta_n \cdot P(z_x, z_y) dz_x dz_y \qquad , \cos\chi > 0$$

$$= \frac{2}{cos\vartheta} \int_{0}^{1} \int_{0}^{\pi} \varepsilon(\chi) \cdot cos\chi \cdot P(z_x, z_y) \cdot \mu_n^{-4} d\phi_n d\mu_n \tag{2.13}$$

, where ε(χ) represents the emissivity from the facet, χ the local emission angle to the facet and $d\phi_n d\mu_n$ the slope distributions components $dz_x dz_y$ converted into solid angles. Note, that direct emission from the sea surface can be blocked either by themselves or by other waves appearing in the emission direction, which leads to unboundedness as ϑ approaches 90° (Masuda et al., 1988; Wu & Smith, 1997). While self-blocking can be excluded by imposing $\cos\chi > 0$, so-called wave-shadowing or slope-shadowing (P. M. Saunders, 1967, 1968) is canceled with a normalization in order to obtain the direct emissivity $\varepsilon^*(\vartheta)$.

In his recent model, Masuda (2006) introduces a shadowing factor s(ϑ), which determines the probability that emission emanates unintermitted from a facet. For the backward unintermitted trajectory, he defined s(180° – ϑ') as the probability for emission to originate from the sky and

$$w(\vartheta) = 1 - (180° - \vartheta') \tag{2.14}$$

as the probability for emission to originate from the sea surface, which he denotes as the weighting function. The angle ϑ' indicates the direction of the direct emission. Masuda attributed the advantage of the weighting function to varying with wind speed due to its dependence on the surface slope distribution. The final surface emissivity ε_{tot} including SESR effects is denoted as

$$\varepsilon_{tot} = \varepsilon^*(\vartheta) + \sum_{i=1}^{\infty} r_i^*(\vartheta) \tag{2.15}$$

, where $r_i^*(\vartheta)$ are the SESR emissivities of order i into direction ϑ.

The current study utilized the above outlined emissivity model of Masuda (2006). An elaborative attempt to implement the entire model was registered to be too costly in the framework of this project[2]. Hence, the emissivity input for the MODTRAN radiative transfer modeling was obtained from the computations published by Masuda (2006). In this concern, direct, first and second order SESR emission were bilinearly interpolated between wind speed and viewing angle and summed up to the total emissivities $\varepsilon_{tot}(\lambda)$ at 3.7 µm, 11 µm and 12 µm. MODTRAN internal processing then interpolates these obtained values over the entire spectral range.

[2] The existing documented, but not functional code is provided with the data DVD, attached to this thesis. A handwritten derivation of direct emissivity after Wu & Smith (1997) is at hand and can be provided upon request.

2.3 The split-window method for surface temperature retrieval from satellite data

Hulley et al. (2011) named three currently available and used techniques for surface water temperature retrieval from TIR remote sensing, of which the split-window method constitutes the most facilely applicable technique due to its modest data and processing requirements. The present section 2.3 encloses the theory of the split-window approach, the evolution of modern split-window algorithms, such as the method used in this study, as well as an overview on the limitations and known problems arising with the method-inheriting idealizations.

2.3.1 The basic concept of the split-window approach

The underlying concept of most studies that aim on retrieving surface temperatures from satellite data refers to the utilization of two simultaneous radiometric measurements, acquired either at different observation angles or in different wavebands of the electromagnetic spectrum. The principle exploited therein corresponds to a proportional relationship between the atmospheric attenuation and the difference in the two radiance measurements (McMillin, 1975). Split-window methods (SWM) are traditionally those methods that use two adjacent channels from operational satellite instruments or airborne sensors. In this context, the following section is designed to briefly summarize the milestones of the development of the nowadays most common forms of the SWM. The description also covers the basic steps of the derivation of the SWM, which are considered to be essential in order to understand the functionality of the SWM for the following chapters.

Saunders (1967) was the first who published results from airborne radiometric measurements of sea surface temperatures at different viewing angles in order to remove the atmospheric effect. Afterwards, Anding and Kauth (1970) proposed a linear relationship between the surface temperature and the radiances in two proper absorption bands in their pioneering study. The theoretical basis for the split-window approach evolved in the first half of the 1970s owing to Prabhakara et al. (1974) and McMillin (1971, 1975), who developed a justification of the split-window approach via the radiative transfer equation. At that time, uncertainties were attributed to a dependence of surface reflectivity on both, angle (Barton, 1983; Chedin et al., 1982) and wavelength (e.g. Prabhakara et al., 1974; McMillin, 1971). McMillin and Crosby (1984) carried out the split-window approach with a dataset from the AVHRR/1 instrument on NOAA 7 and found that the sea surface temperature can be approximated with an accuracy of 1 K.

As discussed earlier in this chapter, extinction of radiation is a wavelength-dependent process. For a cloud-free, non-scattering atmosphere under local thermodynamic equilibrium the radiative transfer equation (2.10) states that the radiance received at the instrument is the sum of the surface radiance attenuated by the atmosphere and the radiance emission along the atmospheric path. By assuming that the water surface emits as a blackbody (Smith et al., 1974), by neglecting the attenuation of other atmospheric constituents along the pathway, by inferring that atmospheric attenuation is solely caused by variations in columnar water vapor and by using the mean value theorem of calculus (Walton et al., 1998) the atmospheric term of the radiative transfer equation (2.10) can be linearized into the following form

$$I_{\uparrow}(\lambda_i, T_i, \theta) = B(\lambda_i, T_S) \cdot t(\lambda_i, \theta) + B(\lambda_i, \bar{T}_a) \cdot (1 - t(\lambda_i, \theta)) \tag{2.15}$$

, where $t(\lambda_i,\theta)$ is the wavelength-dependent atmospheric transmittance, θ the viewing zenith angle, T_S is the temperature of the surface and $\bar{T}_a$ the mean temperature of the atmosphere (c.f. Martin, 2004; McMillin & Crosby, 1984). Recalling that $(1 - t(\lambda_i,\theta))$ equals absorptivity as well as emissivity, equation 2.15 states that the total intensity at the sensor is the sum of the transmitted intensity of any object plus the Planck's function times the total atmospheric emissivity (Petty, 2006). Since the absorption by atmospheric constituents mainly takes place in the lower levels of the atmosphere it is reasonable to assume that the mean atmospheric temperature is the same for two nearby wavebands (McMillin, 1971; Prabhakara et al., 1974). By conserving the assumption that atmospheric attenuation within the window between 10 and 13 μm is mainly caused by columnar water vapor, transmittance per waveband can be approximated by

$$\begin{aligned} t(\lambda_i, p, \theta) &= \exp(-k_i) \cdot X(x_p, \theta) \\ &\approx 1 - k_i \cdot X(x_p, \theta) \end{aligned} \tag{2.16}$$

, where k_i is the absorption coefficient in channel i and X a function of the amount of the columnar water vapor x_p at pressure level p and the viewing angle θ (c.f. McClain et al., 1985; McMillin & Crosby, 1984). Setting up equations 2.15 and 2.16 as a linear equation system for two nearby channels with different central wavelengths and solving the equation system via Taylor expansion of the Planck function has been shown to disembogue into the basic form of the split-window method (Barton, 1995; Walton et al., 1998)

$$T_S = a \cdot T_i + \gamma \cdot (T_i - T_j) + c \tag{2.17}$$

, where T_S is the surface temperature to be estimated, T_i and T_j are the brightness temperatures of channel i and j, and a and c are constants. The gamma parameter or differential absorption term (McMillin, 1975), depending on the author also denoted with Γ, is defined as

$$\gamma = (1 - t_i) \cdot (t_i - t_j) \tag{2.18}$$

Several variations of the algorithm were established via modifications in the retrieval technique of the gamma parameter. Propositions range from constant gamma parameters to proportionalities between gamma and brightness temperature related parameters. Details about operational algorithms and their gamma-parameter are outlined in section 2.3.2.

Coefficients, for algorithms of the form presented in equation 2.17, are typically retrieved in either of two ways:

(1) A semi-empirical approach that uses multi-linear regression of brightness temperatures derived from radiative transfer modeling (e.g. Hulley et al., 2011; Závody et al., 1995) against an estimated surface or bottom-of-the-atmosphere temperature. The data input for the simulations is usually provided by radiosonde measurements or by large scale climate modeling reanalysis.
(2) A statistical approach in which the remotely sensed brightness temperatures are regressed against in situ measured temperatures from buoys, ships or whether stations (e.g. Kilpatrick et al., 2001).

It is important to notice that the first approach delivers surface water temperatures closely related to real skin-surface temperature, while the second approach is tuned to the foundation temperature (or historically “bulk” temperatures) (Donlon et al., 2007). Water temperatures are however known to vary diurnally and nonlinearly within the uppermost 10m of the water surface (Donlon et al., 2002b, 2007; Minnett et al., 2011), depending on the mixing dynamics within the water basin. This problem is apprehended in section 2.3.3, again.

Now, that the basic concept of split-window algorithm has been outlined, section 2.3.2 will review the most important stages in the development of operational split-window algorithms with a focus on AVHRR data.

2.3.2 Evolution of operational split-window methods

The first operational algorithm for the NOAA AVHHR instrument series was proposed by McClain et al. (1985) and utilized AVHRR channels 3, 4 and 5. This so-called multichannel SST (MCSST) algorithm assumes a linear dependence of the differences in brightness temperatures among AVHRR channels, i.e. a constant gamma in equation 2.17. The gamma parameter of the MCSST was estimated from a radiosonde dataset of temperature and humidity profiles measured over the ocean. The great advantage of the MCSST is that once its constants are determined, the equation remains invariant (Martin, 2004). One of the major improvements, implemented in a later stage of the MCSST, incorporated a viewing zenith angle correction after Llewellyn-Jones et al. (1984) in order to account for the change of the atmospheric path with different observation angles (Cornillon et al., 1987). With the cross-product algorithm (CPSST), Walton (1988) proposed a proportional relationship between gamma and the brightness temperature in order to improve the atmospheric correction. The most widely used form of the split-window technique in operational mode today, refers to the nonlinear SST (NLSST) algorithm presented by Walton et al. (1998)

$$T_S = a_0 + a_1 \cdot T_i + a_2 \cdot \gamma \cdot \left(T_i - T_j\right) + a_3 \cdot \left(T_i - T_j\right) \cdot (sec\theta - 1) \tag{2.19}$$

, where T_S is the water surface temperature, a_x the split-window coefficients and θ the viewing angle. The last term on the right hand side of equation 2.19 denotes the viewing angle correction. In the NLSST algorithm the gamma parameter is assumed to be proportional to a first-guess SST value obtained from either in situ measurements (e.g. Kilpatrick et al., 2001) or atmospheric modeling (e.g. Hulley et al., 2011; Závody et al., 1995).

The operational SST products of MODIS and AVHRR incorporate the NLSST. Whereas the MODIS product uses radiosonde measurements and ECMWF reanalysis data for the computation of the regression coefficients (c.f. Brown & Minnett, 1999), the AVHRR product uses in situ measurements of an intergovernmental buoy network (c.f. Kilpatrick et al. 2001). Both models, for MODIS and AVHRR data respectively, derive different pairs of coefficients for different atmospheric regimes, and include sophisticated statistical modeling, coefficient weighting as well as extensive level-based quality flagging of the computed SSTs. However, the surface temperature retrieval algorithms for MODIS and AVHRR, respectively, provide sets of coefficients, which are designed for the prediction of ocean water surface temperatures on a global scale. In this context the next section is designed to introduce recent approaches to access LSWTs with regionally tuned split-window coefficients.

2.3.3 Capabilities and challenges of operational split-window techniques and requirements for lake surface water temperature algorithms

More recently, studies revealed the potential of the split-window technique for exploiting lake-surface temperatures of larger inland-water bodies as climate proxies for regional studies (e.g. Oesch et al. (2005); Schneider & Hook (2010) and references therein). In this context it is reasonable to assume that split-window models tuned to regional climate conditions would deliver superior results over the global algorithms. For a study on Lake Tahoe and Salton Sea, two lakes in the state of California (USA), Hulley et al. (2011) received RMSE improvements of 0.3 - 0.4 K compared to the globally adjusted operational MODIS and AASTR split-window products.

In general, the errors margins of operational models have constantly been diminished by improvements of the initial regression equation and in the subsequent quality assessment, during recent years. Requirements for operational water surface temperature retrieval algorithms generally demand nominal accuracies below $< \pm 0.5$ K (e.g. $< \pm 0.4$ K on oceanic scales (Jeffery & Vazquez, 2011) to $< \pm 0.2$ K for lake water temperatures (GCOS, 2006)).

Limitations to the global approaches arise especially for atypical atmospheric and oceanic conditions, which violate the assumptions of the underling model. Examples refer to deviations from the global mean atmospheric state (e.g. unusual atmospheric water vapor or temperature profiles), which is represented in the first-guess temperature, as well as to upper oceanic water stratification. While atmospheric deviations are less likely to occur for a regionally tuned algorithm, as it is used in this study, water stratification in lakes has been identified as a major challenge to accurate surface water temperature estimations (Merchant et al., 2006; Oesch et al., 2005). Radiometric water temperature measurements access only the upper approximately 10 μm of the oceanic skin layer, while in situ temperatures from ships, buoys or measurements stations are usually collected in 0.5 to 5 m below the water surface (Emery et al., 2001). As for example extensively discussed in Donlon et al. (2002, 2007), Emery et al. (2001) and Minnett et al. (2011) the upper 10 to 20 m of the ocean possess a complex and diurnally varying temperature structure, mainly driven by wind and shear stress from water flow and swell. Diurnal stratification on calm days is able to impose fluctuations around 2K within the uppermost meters of the water body (c.f. Donlon et al. 2002), which makes a correction for comparing bulk and in situ measurements highly desirable. Minnett et al. (2011) compared in situ SST measurements from the marine-atmospheric emitted radiance interferometer (M-AERI) with synchronously measured bulk temperatures in order to retrieve a correction for the thermal stratification. In order to reduce the skin-effect, the model of Minnett et al. (2011) incorporated into

the algorithm implemented in this study. This model formulates an exponential dependence of the skin-effect on wind speed and is

$$\Delta T = -0.130 - 0.724 \cdot \exp(-0.350 \cdot U_{10}) \tag{2.20}$$

, where ΔT is the skin-bulk temperature difference imposed by the skin-effect and U_{10} the wind speed in 10m height.

In addition to the abovementioned challenges for modern SST (and LSWT) algorithms there are numerous other triggers for uncertainties. Many of them introduce variability into the mean atmospheric model-state and therefore violate the model assumptions that underlie the split-window approach. Some of them are listed below

- Injection of atmospheric aerosols due to large volcanic eruptions, such as Mount Pinatubo in 1992 (Kilpatrick et al., 2001; Li et al., 2001; Walton et al., 1998)
- Variability in the lower atmospheric state due to undetected low level fog, especially in the early morning during summer and for in situ temperatures close to 4°C, which were attributed to be more susceptible to ambiguities with warm low clouds and fog (Li et al., 2001).
- Uncertainties from sub-pixel clouds and cloud shadowing (Castro et al., 2010; Hulley et al., 2011; Oesch et al., 2005)
- Uncertainties evolving from littoral mixed land-water pixels (Michael Riffler, results not published yet)
- Sensor inheriting uncertainties from the calibration and sensor noise (Donlon et al., 2007; Robel, 2009)

Chapter 3

Data & Study Site

After the physical principles involved in radiative transfer modeling and LSWT retrieval were clarified, chapter 3 wraps a specification of the lakes, surface water temperatures are computed for, as well as an introduction of the available data archives. The first three sections encompass the in situ database, the AVHRR data archive and the ECMWF database. The last section summarizes additional archives that have been accessed during the course of the study for minor adjustments of the model.

3.1 The study site and the in situ database

Switzerland is located in Central Europe and dominated by an alpine landscape with various lakes formed during the last alpine glacial period. Figure 1 shows a masked map of Switzerland, where only the Swiss boarders and the locations of the largest inland water bodies on Swiss territory are displayed. MODTRAN radiative transfer simulations were computed for six, on the map marked and named locations in the central areas of Lake Constance (BDS), Lake Geneva (GFS), Lake Lucerne (VWS), Lake Neuchâtel (NBS), Lake Lugano (LGS) and Lake Zurich (ZUE). The lakes were selected primarily for their comparatively large total lake area and for their spatial distribution. Firstly, central water pixels in large lakes can be assumed to avoid pixel mixing with lakeshore pixels. Secondly, large lakes can be assumed to play an important role as a regional climate archive (cf. Adrian et al., 2010), which can allow split-window coefficients derived for one large lake to be used for nearby smaller lakes, as well (personal communication with Michael Riffler). The spatial distribution of the

selected lakes would support this overlapping derivation of split-window coefficients for smaller lakes in the expanded catchment of nearby larger water bodies.

Table 1: List of the six Swiss inland water bodies considered in the MODTRAN radiative transfer simulations and the split-window coefficient derivations.

Lake ID	Lake	Latitude [°N]	Longitude [°E]	Elevation a.s.l. [m]
BDS	Lake Constance	47.57	9.49	396
GFS	Lake Geneva	46.42	6.42	372
LGS	Lake Lugano	45.91	8.56	194
NBS	Lake Neuchâtel	46.96	6.92	429
VWS	Lake Lucerne	47.03	8.37	433
ZUE	Lake Zurich	47.22	8.71	406

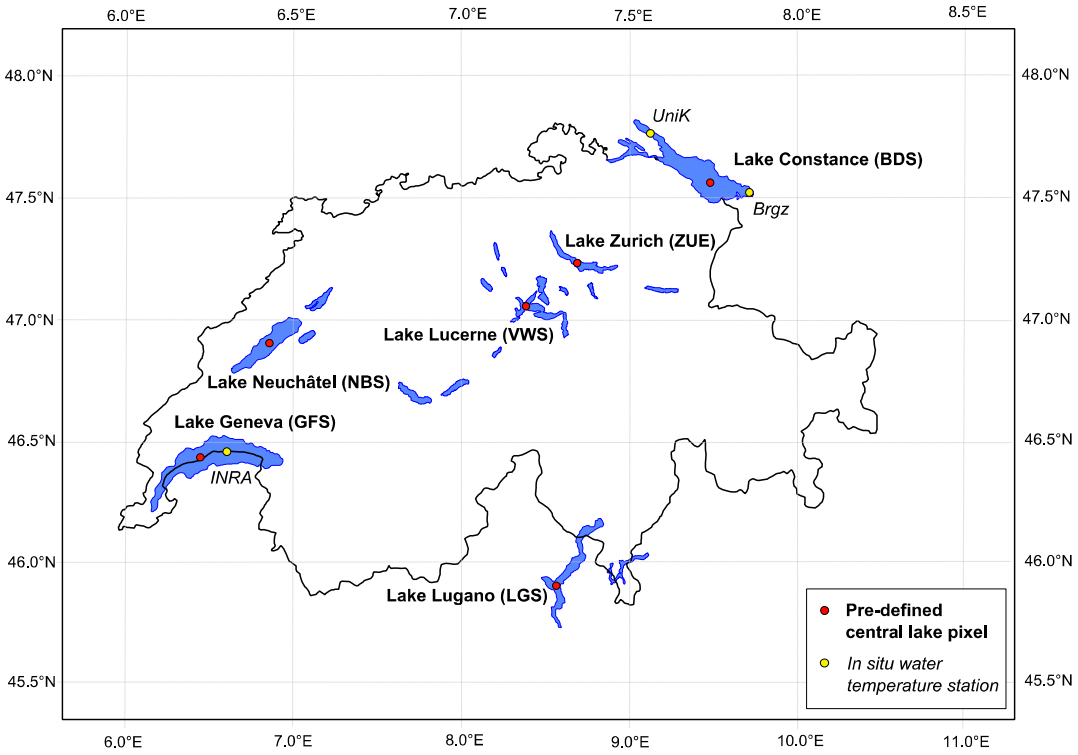

Figure 1: Map of large inland water bodies in Switzerland. Six named (bold) and marked (red dot) positions in Lake Constance, Lake Geneva, Lake Lugano, Lake Lucerne, Lake Neuchâtel and Lake Zurich are specified as representative lake pixels in the radiative transfer simulations with MODTRAN. The positions of the in situ temperature stations (INRA, Brgz, UniK) at Lake Geneva and at Lake Constance are marked with a yellow dot.

For the success of this study, several Swiss cantonal administration offices and universities provided in situ lake water temperatures for a period between 1989 and 2012. The entire collected archive

consists of 25 datasets, each provided with a specific depth profile and temporal resolution[3]. The heterogeneity between the datasets, due to inconsistent data formats and especially non-standardized measurement depths throughout the cantonal institutions, accompanied with the low temporal resolution of lake temperatures, remains a general challenge for lake temperature studies (see discussion section 5.5). The final comparison of LSWTs derived from the MODTRAN- and the RTTOV-algorithm is based on three validation data sets, two of them acquired at Lake Constance (UniK, 47.762 °N / 9.131 °E; Brgz, 47.507 °N / 9.748 °E) and one at Lake Geneva (INRA, 46.453 °N / 6.589 °E). The locations of the three stations are illustrated in Figure 1. The decision for these datasets corresponds to the available amount of validation data points, supplied with a daily or finer temporal resolution at these locations. All selected datasets partially coincide with the operational period of the selected satellite platforms NOAA 17 and NOAA 18, which allows a comparison between RTTOV's and MODTRAN's simulated LSWTs with reliable statistical analysis and inference.

3.2 The AVHRR database

Satellite data are well known to provide an excellent source for monitoring geophysical parameters over long periods (GCOS, 2006). In this respect, the continuously growing AVHRR dataset of the University of Bern delivers an appreciated basis for the derivation of long-times series from the 1980s to the present day (e.g. Hüsler, 2012). The following overview on the AVHRR sensor and on the RSGB's database is designed to grasp the eligibility of this long time series for LSWT derivations.

Table 2: Approximated spectrometric characteristics of the three operational AVHRR instruments (Hüsler et al., 2011).

Channel	AVHRR/1	AVHRR/2	AVHRR/3
1	0.58 - 0.68 µm	0.58 - 0.68 µm	0.58 - 0.68 µm
2	0.73 - 1.10 µm	0.73 - 1.10 µm	0.73 - 1.00 µm
3A	-	-	1.58 - 1.64 µm
3B	3.55 - 3.93 µm	3.55 - 3.93 µm	3.55 - 3.93 µm
4	10.50 - 11.50 µm	10.30 - 11.30 µm	10.30 - 11.30 µm
5	*Ch. 4 repeated*	11.50 - 12.50 µm	11.50 - 12.50 µm

The first AVHRR sensor was originally designed to monitor cloud patterns on Earth within four spectral channels in the VIS and NIR in the mid 1970s (Hastings & Emery, 1992). The sensor is

[3] A full overview of the available in situ datasets is given in Appendix B.

operating onboard of the NOAA Polar-Orbiting operational Environmental Satellites series at an altitude of approximately 833 km above sea level and possesses a spatial resolution of 1.1 km² at nadir and a swath width of 2700 km into off nadir direction. Table 2 summarizes the radiometric specifications of the instrument throughout its development stages (c.f. Hüsler et al., 2011). While AVHRR/1, the first version of the AVHRR instrument, was originally designed to obtain radiation in four bands of the electromagnetic spectrum, AVHRR/3, the most recent version, provides six channels, sensitive to radiation in the visible, near-infrared and thermal-infrared. The sensor's improvements made it a multifunctional monitoring tool, with tasks far beyond the originally intended scope. Within its lifespan, the AVHRR instrument series has featured scientific investigations on the composition and development of clouds (Turner & Warren, 1989), sea ice motion (Emery et al., 1991), atmospheric aerosols (Emili et al., 2011; Riffler et al., 2010), water vapor contents (Sobrino et al., 1999), sea surface temperatures (Kilpatrick et al., 2001), land surface temperatures (Tomlinson et al., 2011), snow detection and analysis (Hüsler, 2012) and on vegetation (Kogan et al., 2003). As illustrated in the bar chart (Figure 2), AVHRR was mounted to various platforms throughout its evolution. Starting with TIROS-N at first launch, the sensor was continuously carried by the Polar Orbiting Environmental Satellites (POES) of NOAA or more recently by the Meteorological Operational satellite programme (MetOp) of the European Space Agency (ESA) and the European Organisation for the Exploitation of Meteorological Satellites (EUMETSAT). Launches of MetOp-B in 2012 and MetOp-C in 2016 are planned to be equipped with AVHRR/3 and thus to extend AVHRR's acquisition period at least into the year 2020 (http://www.esa.int).

The RSGB database of observations from the advanced very high resolution radiometer (AVHRR) is one of the most comprehensive in Europe, which offers a unique potential for long-time studies of various kinds (c.f. Hüsler et al., 2011). Available satellite data range from 1981 to up-to-date scenes. Additionally to the data gained from the local receiving station in Switzerland (46.93 °N / 7.41 °E), the RSGB has put much effort into collecting early data from other institutions in order to build up a long time series of continuous AVHRR (see Hüsler et al., 2011, for details). A comprehensive overview of the RSGB database, including a data description as well as details on the reception, collection and calibration are provided in Hüsler et al. (2011).

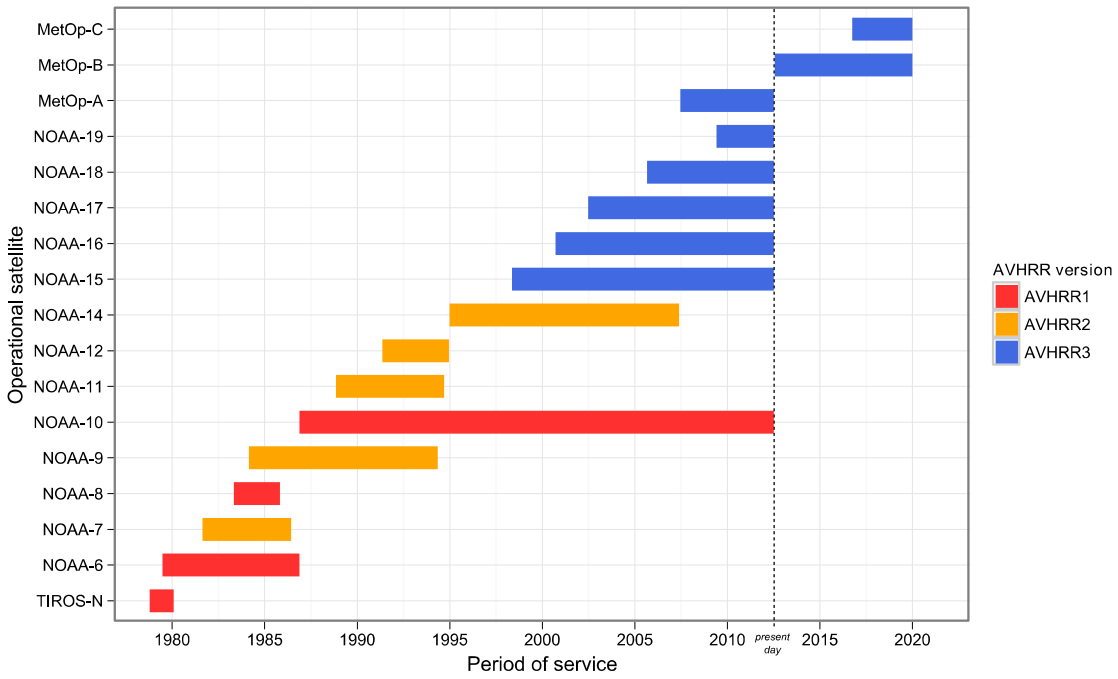

Figure 2: Past, present and future service periods of the different AVHRR sensors (data are obtained from http://wdc.dlr.de/sensors/avhrr/). Launches for MetOp-B and MetOp-C are scheduled for the second half of 2012 and for 2016, respectively. AVHRR/3 maintenance is planned to be extend at least into the year 2020 (http://www.esa.in).

The data input for the LSWT calculations is based on a subset of the Alpine Region, obtained from radiometrically corrected and geometrically ortho-rectified NOAA AVHRR Level 1B data, which were reprojected onto the WGS84 spheroid. This subset from the European alpine region covers an area between 41° - 50°N and 0° - 17°E, which spaciously integrates the study site. The radiometrically corrected and ortho-rectified AVHRR data of one observation consist of one zipped file with pixel-wise radiometric information of AVHRR channels 1 to 5 as well as one zipped geometry file containing the pixel-wise viewing and solar geometry at the acquisition time, each existing with an equally named header file with the .ers-extension that contains file characteristics[4]. The filename consists of a unique satellite identifier, the observation date as well as the observation time in hours and minutes and a suffix which discriminates between geometric and radiometric data, respectively. A typical example of an ortho-rectified AVHRR-file and its corresponding header file is shown below.

N17_05apr08_1900_rect.ers

N17_05apr08_1900_rect.bz2

[4] The data are available on /data/sensor/avhrr/products/realtime_mr/SST/rectified/.

3.3 Atmospheric profiles from the ECMWF database

The following section gives a brief overview of the origin of the climatology data, used for the MODTRAN radiative transfer simulations in this study. The information provided here, are extracted from the official website of the European Center for Medium-Range Weather Forecasts (ECMWF) (http://www.ecmwf.int). The ECMWF is an intergovernmental organization, which produces high-quality operational medium-range numerical whether predictions. The ECMWF website also hosts detailed reports about processing modalities, parameter and data availability as well as the milestones and the future aims of the project.

Forecast and analysis fields for this study were accessed from the operational global ECWMF Integrated Forecast System (IFS). The multi-component model provides a deterministic forecast as well as a 51-member ensemble, which combines different sorts of observations and model information in order to produce a consistent best estimate of the atmospheric and oceanographic state (Persson, 2011). The available dataset of the Product Set I of the ECMWF deterministic forecast model are on hand for the years 2000 to 2010, hence offering a period of eleven years of coinciding climatology and satellite data. The forecast dataset possesses a daily temporal resolution (i.e. data at 12 UTC each day) and covers an area between 45° - 48°N in latitudinal direction and 4.95° - 10.05°E in longitudinal direction with a 0.15°-grid-resolution, such that overlapping with the satellite and the in situ data is guaranteed.

Table 3: List of the parameters obtained from the ECMWF integrated forecast system Product Set 1. Parameters accessed and utilized for lake surface water temperature retrieval are indicated with a dot (●) in the right column.

Parameter type	Parameter	Abbreviation	Unit [SI]	Utilization
Integrated or single level parameter	Surface pressure	SP	hPa	●
	Mean sea level pressure	MSL	hPa	
	Total cloud cover	TCC	%	
	Low cloud cover	LCC	%	
	Medium cloud cover	MCC	%	
	High cloud cover	HCC	%	
	10 m U-velocity	10U	m/s	●
	10 m V-velocity	10V	m/s	●
	2 m dew point temperature	2D	K	●
	2 m temperature	2T	K	●
	Skin temperature	SKT	K	●
	Total column water vapor	TCWV	g/cm²	●
	Total column Ozone	TCO3	DU/100	●
Pressure level parameter	Pressure (21 levels)	P	hPa	●
	Relative humidity (21 levels)	RH	%	●
	Temperature (21 levels)	T	K	●

Each time step includes at-the-time atmospheric information about the relative humidity and temperature at 21 predefined pressure levels, as well as 13 additional parameters on cloud coverage, trace gas composition and the state of the boundary layer. The 21 pressure levels range from the 1000-hPa-level to the 1-hPa-Level with a logarithmic scaling. Table 3 lists an overview of the available ECMWF parameters. A utilization of the parameter for the radiative transfer modeling or other aspects of the LSWT retrieval is indicated[5].

[5] The cloud cover parameters provided with the single level parameters were not exploited for the analysis, since the reliability for cloud masking purposes could not be ensured (personal communication with Michael Riffler).

Chapter 4

Methods & Implementation

Chapter 4 basically contains a description of the implemented algorithm from the input of the data to the final LSWTs. Figure 3 displays scheme of the order of the steps as well as the main components of this algorithm, and will be referenced at each of the steps during the course of chapter 4. At first, section 4.1 gives an overview on the software tools utilized for the realization of the algorithml and the visualization of the results. Afterwards, section 4.2 follows with a review of the MODTRAN radiative transfer model, which embodies the core piece of the algorithm. Section 4.3 describes the arrangement of the input parameters for the MODTRAN RT model, and guides through the implementation of the MODTRAN simulations. Section 4.4 concentrates on the computation of the split-window coefficients as well as on the calculation of LSWTs from actual AVHRR observations. Readers with some small background in programming are advised to consider the documented IDL code as supplementary material to chapter 4. The documentation might give additional insights to single steps of the algorithm in a greater depth. Thereby, the header of each function gives detailed information on the calling sequence, the name, the purpose, the input and output parameters, and other procedures that are being called within this function. A full list of all functions in use can be accessed in Appendix A. The code is provided with the data DVD[6].

[6] Directory name: /IDL/

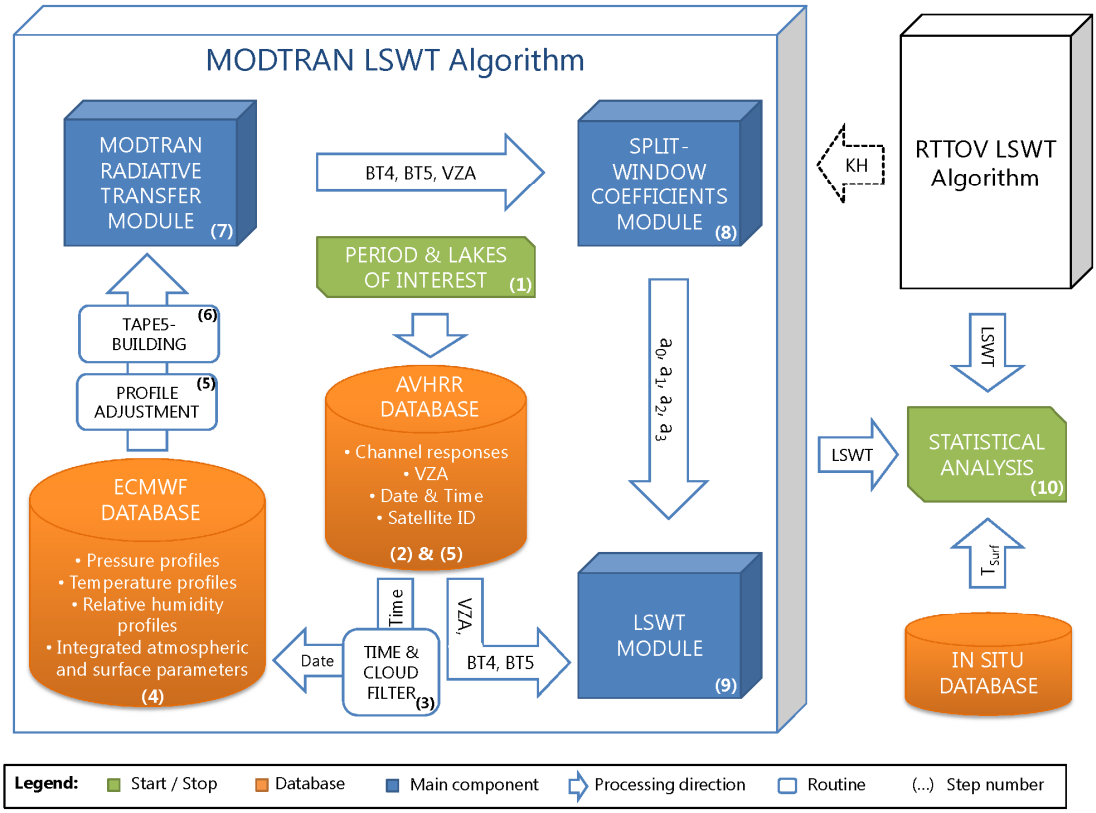

Figure 3: Simplified scheme of the implemented algorithm. The processing starts with a characterization of the target lakes and the processing period (1) and ends with the statistical analysis (10). Step numbers at the bottom of each component indicate the stages at which the specific component is run. The AVHRR database is accessed twice, once for cloud masking in the initial stage (2) and once for lake surface water temperature (LSWT) computations a late stage (5). Parameters are denoted as follows: BTx denote the brightness temperature of channel 4 and 5 respectively, VZA is the viewing zenith angle of the sensor, a_0 to a_3 denote the split-window coefficients, TAPE5-Building symbolizes the input-file generation for the MODTRAN simulations, LSWT is the simulated lake surface water temperature of MODTRAN and RTTOV respectively, and T_{surf} the actually measured in situ water surface temperature. KH in the dashed black arrow summarizes the transfer of know-how from the existing and operational RTTOV LSWT algorithm into the MODTRAN LSWT algorithm.

4.1 Tools for data processing and data visualization

The performance of radiative transfer simulations, the calculations of split-window coefficients and the derivation of LSWTs are three computer-intensive tasks. Professional software is necessary in order to solve the radiative transfer equation and the multi-linear regression for the available amount of data. The key-tool for joining the procedures from the data import to the final LSWTs was the Interactive Data Language (IDL) (ITT, 2009), which is a commonly used programming languages in remote sensing applications. Radiative transfer simulations are carried out with the commercial Moderate Resolution Atmospheric Transmission model (MODTRAN) (Berk et al., 2008). Since the

MODTRAN model is a tool of complex nature, designed for a variety of applications in atmospheric physics, section 4.2 gives a brief insight into the functionally of the model in general sense. The MODTRAN radiative transfer model is called by means of the graphical IDL front-end MODO (Schläpfer, 2011). The graphical output is mainly performed with the open source statistical programming language R (R Development Core Team, 2012), which included an extensive utilization of the ggplot2 package (Wickham, 2009). The work chart (Figure 3) was made with the vector graphics editing software Inkscape (www.inkscape.org). The visualization of the data involved data export by IDL into a common ASCII format and data import by R from the same format.

4.2 Development and general functionality of MODTRAN

This section is intended to give some insights into the Moderate Resolution Transmission (MODTRAN) program. Since MODTRAN does not only represent a radiative transfer model, but also a multi-version project, developed over four decades, a comprehensive technical report that explains the entire model does not exist. All information that are supplied about MODTRAN 5.2 in this study are based on a combination of reference manuals and technical reports (Berk et al., 2005, 2008; Kneizys et al., 1996), the FAQ on the official website of MODTRAN5 (http://modtran5.com/faqs/index.html) and frequent correspondence with the support (modtran@spectral.com) as well as the lead developer Alexander Berk in person.

MODTRAN's precursor, the Low Resolution Transmission program (LOWTRAN), was developed by the U.S. Air Force Geophysics Laboratories (now Air Force Research Laboratories) with a spectral resolution of (20 cm^{-1}) in the early 1970's. LOWTRAN was improved and modified into several updated versions and was re-named into MODTRAN with an upgrade of the band model to a 1.0 cm^{-1} resolution by Spectral Science, Inc. (SSI). Afterwards, the Air Force Research Laboratories took over the support and validation, while SSI has continued MODTRAN's development. The MODTRAN5 package provides six cloudless standard atmospheres for different seasons and climatic zones with distinct differences in their atmospheric compositions and their temperature profiles (Kneizys et al., 1996). Additionally, it provides numerous options for the user to define the type and the accuracy of the model, the constitution of the atmosphere including cloud coverage, the viewing geometry, the light source and the surface properties with any specific set of parameters. These options for atmospheric tuning have extensively been used in the course of this study.

The functionality of MODTRAN follows the discrete layer approach. This means, that MODTRAN integrates over the radiance contribution of a finite amount of homogeneous layers in order to obtain the transmittance (or radiance) for the specified atmosphere. Spectroscopic line compilation was derived from the High-resolution Transmission molecular absorption database (HITRAN) (Rothman et al., 2009) and integrated into the MODTRAN 1.0 cm^{-1} band-model. The integration surpasses a layer-wise adjustment of the absorption coefficients for the pressure and temperature variations, a subsequent calculation of the layers' optical depths and the computation of the total radiance with the radiation transfer equation (Kneizys et al., 1996; Selby & McClatchey, 1975).

The input for every MODTRAN simulation consists of one single input file, the tape5-file. The tape5-file enables the user to set parameters, to define user-specific atmospheres, to specify information about additional files and to trigger different model-types. The tape5-file is split into several CARDs of different categories. Six cards are compulsory for every tape5-file in order to initialize a MODTRAN simulation, while a variable number of sub-cards can be switched on and off, depending on user's objectives. A full overview of the CARDs accessed and set for the RT simulations, the parameters and their position in the tape5-file, as well as of a short description of each parameter's purpose can be found in the MODTRAN_param.xls on the data DVD provided with this study. The tape5-files are stored locally and jointly with the MODTRAN output-files. The number of output-files for one simulation depends on the parameters set in the tape5-file, but by default consists of six files with the following file extensions: .tp6, .tp7, .7sc, .plt, .psc, .chn.

4.3 Radiative transfer modeling with MODTRAN

Section 4.3 covers the steps (1) to (4) of the MODTRAN LSWT algorithm, symbolized by the blue box in Figure 3. This algorithm has to ensure that the ECMWF climatology is selected for the specified target lake pixels, that cloudy or corrupted dates are omitted from the simulations, that temporally and spatially matching data are selected from the ECMWF, and that the information derived from the database are correctly transferred and positioned into the tape5-file, before actual RT simulation can be started. The following section is designed to cover this procedure descriptively and guides along the cornerstones of the algorithm. MODTRAN-inexperienced readers are advised to keep the documented code, the parameter summary table provided on the attached data DVD and the official MODTRAN manual (Berk et al., 2008) handy, in order to obtain the best possible comprehension of the processing steps and the used parameters.

4.3.1 Import and selection of the AVHRR data

The import of the AVHRR data and the selection of appropriate data is a necessary step in radiative transfer simulation. Depending on the amount of satellite data considered, this step can be relatively time-consuming. The complete data import, the selection of the appropriate dates, the creation of the input-files as well as the radiative transfer simulations are performed with one comprehensive routine. At startup this routine needs to be called with a starting and an ending date for the requested simulation period. Then, in a first step, a sub-routine imports the lake identifiers (ID) of the favored lakes, the geographical coordinates of the target lake pixel and the elevation of the lake from an input-file almost identical to Table 1. Afterwards the algorithm imports the CO_2- (NOAA ESRL, ftp://ftp.cmdl.noaa.gov/ccg/co2/trends/co2_mm_mlo.txt) and the solar-constant-tables (Wang et al., 2005). In a second and third step (see Figure 3), the algorithm accesses the AVHRR database and selects observations based on two criteria:

(1) The AVHRR observation lies within a centered 4-hour-window around 12:00 UTC[7]
(2) At least one of the specified target pixels possesses valid and cloud-free spectrometric information

The first criterion is tested with a sub-routine that imports the AVHRR filenames of one month into an array, extracts the temporal information from the filenames and verifies whether the observations are located within the four-hour-window. If the AVHRR data passed the first test, another sub-routine extracts the compressed AVHRR-data files into a temporary directory. Subsequently, the algorithm imports the data iteratively, identifies the target pixels in the gridded AVHRR and proceeds with a verification of the second criterion[8]. The verification of the second criterion follows a two-step testing. The first step extracts a 5x5-pixel-patch, where the target pixel is centered within this patch, computes a simple ratio of the spectrometric information of channel 1 over channel 2 per pixel and verifies whether the threshold of at least 5 pixels in the 5x5-patch is smaller than a predefined threshold of 0.08 (threshold determined from personal communication with Dr. Michael Riffler). The test utilizes the discriminating spectral characteristics of water and clouds in the EM bands covered by AVHRR channel 1 and 2. The reflectivity of water in the near infrared band of AVHRR channel 2 is generally very low compared to the reflectivity of clouds in the same region. The second test follows the suggestions of Saunders and Kriebel (1988) for a spatial coherence cloud test. Therefore,

[7] Remember, that the ECMWF-profiles are provided for 12:00 UTC with a daily resolution. The variable atmospheric water vapor column is assumed to remain sufficiently constant within this window. The four-hour-window is a tradeoff between availability of sufficient AVHRR data and accuracy. The tolerance-window can be varied as in the input parameters of the sub-function.
[8] A full description of the import and adjustment of the ECMWF climatology is provides in section 4.3.2.

the 5x5-pixel-patch is once again tested with a channel-2-over-channel-1-ratio against a threshold of 1.0 in order to distinguish between land and water pixels. This is necessary because target pixels of narrow lakes might not entirely be surrounded by pure water pixels. Subsequently, the obtained small-scale land-water-mask is used to check, whether the standard deviation of the valid water pixels surpasses a value of 0.2, as suggested by Saunders and Kriebel (1988). The test exploits the small variability that can be expected for undisturbed and homogenous water surfaces. In addition to the threshold-based test, the 5x5-patches are verified against zero values, which can appear for corrupted images or in case only parts of the entire scene were obtained from the sensor.

The result of the time filter and the cloud check is a point-in-time-specific data mask that discriminates between valid, cloud-free target pixels and invalid target pixels for all AVHRR observations in the four-hour-window around noon. This mask is applied to the daily ECMWF database in order to implement only cloud-free re-analysis days into the MODTRAN simulations.

4.3.2 Selection, adaptation and assignment of the ECMWF profiles

In step four, the MODTRAN LSWT algorithm imports the yearly ECMWF data[9]. Yearly in this contexts means that the four-dimensional data arrays hold daily surface and profile parameters for one entire year. Remember, that the ECMWF climatology supplies profiles starting at the 1000-hPa-level. The lakes' surface-water levels are however located at heights, where the pressure is frequently lower than 1000 hPa and sometimes even lower than the second ECMWF pressure level at 925 hPa. For matters of consistency the number of atmospheric levels was decided to be kept constantly at 21 levels for every simulation, which can require an adjustment of the ECMWF profiles in order to fit their corresponding ground parameters, as illustrated as step five in Figure 3.

For these data that are not masked from the cloud and time filter, the algorithm now selects the corresponding daily ECMWF data. In a next step, the algorithm adjusts every first ECMWF-profile-level at 1000 hPa for the altitude and the ground pressure of the target pixels in question. In this context, the entire 1000-hPa-profile-level is overwritten with the surface ECMWF parameters, i.e. the surface pressure replaces the first pressure level, the 2m-boundary-layer-temperature replaces the first temperature level, etc.. Thereby the relative humidity for the surface level is approximated from the dew-point-temperature with the August-Roche-Magnus approximation ([p.44] Etling, 2008)[10], because the ECMWF surface parameters do not contain relative humidity information, directly.

[9] ECMWF data directory: /data/results/riffler/atm_profiles/
[10] Etling abbreviates the approximation with Magnus-formula.

Finally, the algorithm indentifies the first of the remaining pressure levels that is larger than the newly set ground pressure and, if necessary, linearly interpolates the profile parameters to matching 21 levels again. The altitude of each atmospheric level is approximated from by means of the hypsometric formula from the corresponding the pressure level ([p.92] Petty, 2008).

When the adaption of ECMWF profiles is finished, the modified profile is assigned to the MODTRAN input file on CARDs 2C and 2C1 of the tape5-file, where the specified parameters are going to "overwrite" the standard mid-latitude profile of water vapor, temperature, altitude and pressure. The concentrations of the remaining atmospheric constituents are determined from one of two of MODTRAN's internal standard atmospheres for summer and winter mid-latitudinal conditions. The determination between summer and winter standard atmosphere follows an evaluation of the current day of year. Summer profiles are adopted for dates between April, 7th and November, 8th, respective winter profiles for the rest of the year. Onset and end of the seasons are obtained from the mean date between the vernal equinox and the summer solstice for defining the start of the summer period, and the mean date between the autumnal equinox and the winter solstice for defining the start of the winter period. Solstices and equinoxes are obtained as mean values from the last 120 years from the NASA database (http://aom.giss.nasa.gov).

The highest profile level at 1 hPa corresponds approximately to an altitude of 50 km, whereas POES satellites operate in altitudes at ~ 830 km (Robel, 2009). Since most of the atmospheric attenuation takes place in the troposphere and stratosphere[11], this altitudinal difference would only slightly affect the radiative transfer simulation incase the line-of-sight-geometry is kept constant. MODTRAN, however, resets the altitude of the observer (i.e. the satellite) to the highest specified profile, such that the viewing geometry as well as the atmospheric path would be modified[12]. For this reason, the algorithm adds six supplementary levels at constant atmospheric altitudes (50, 75, 100, 200, 400, 830 km), for which the MODTRAN mid-latitudinal standard concentrations of the atmospheric constituents remain unchanged.

[11] The atmospheric concentrations run against zero, when approaching the satellite's operating altitude.

[12] The supplement of atmospheric levels between the highest ECMWF profile and the satellite altitude is necessary in order to obey the original line-of-sight-geometry between the sensor and the target. In case ECMWF profiles are consigned solely without the supplementary levels, MODTRAN rescales the sensor height to the highest user-specified atmospheric level, i.e. ~50 km in the present case. This however leads either to a significant deviation from the original VZA and thus from the original atmospheric path or to a change of the latitudinal and longitudinal positioning of target and/or sensor. The insertion of those gap-filling levels tributes to the extinction within upper atmospheric levels on one hand and ensures a rather realistic sensor-target-geometry on the other hand.

4.3.3 Running MODTRAN with user-specified tape5-files

The derivation of the tape5-input-file is a crucial task in the preparation of the radiative transfer simulations with MODTRAN (steps six and seven in Figure 3). Only a valid combination of parameters exactly placed at the location that is reserved for the corresponding parameter will lead to a full run of the MODTRAN code. The atmospheric conditions for one radiative transfer simulation in this study are specified via CARDs 1, 1A, 1A3, 2, 2C, 2C1, 3, 3A1, 3A2, 4, 4AL1, 4L2 and 5 of the tape5-file [13]. In order to capture a broad range of satellite-target geometries and surface temperatures, RT simulations were performed for eight viewing zenith angles [0°, 15°, 30°, 40°, 45°, 50°, 55°, 60°] and five surface temperature variations between -10 K and + 10 K (Hulley et al., 2011), resulting in forty simulations and forty tape5-files per input date. Thereby, the surface temperatures are obtained from varying the ECMWF skin-temperatures by a 5-K-increment within the aforementioned range.

The tape5-files are generated via an iteration over the lake-target-pixels, the five ECMWF surface temperatures and over the eight viewing zenith angles. The corresponding ECMWF profile as well as the surface parameters are transferred into the tape5-file and are put into their specific format and location. The total wind speed is calculated as the Euclidian distance of the u- and v-component from the ECMWF surface parameters. Subsequently, total wind speed and viewing zenith angle are used to generate a spectral-albedo-file from the bi-linearly interpolated emissivity of Masuda (2006). The computation of the albedo exploits the fact that albedo and emissivtiy sum up to unity (Petty, 2006). The total column water vapor and the total column ozone, provided by the ECMWF reanalysis data, are simply assigned as the corresponding tape5-parameter. MODTRAN uses them for rescaling of the humidity profile and the standard ozone profile. A monthly carbon dioxid concentration for Switzerland is approximated form a longtime record of the NOAA Earth System Research Laboratory on Mouna Loa, Hawaii, USA (http://www.esrl.noaa.gov/gmd/ccgg/trends/). The exact regional CO_2-concentration is of minor importance for atmospheric attenuation, when compared to the concentration of water vapor (c.f. Petty, 2006). Hence, this approximation is considered to deliver reliable results. In order to receive sensor-characteristic brightness temperatures, MODTRAN is provided with the spectral-response file obtained from the NOAA KLM User's guide (Robel, 2009).

The geometry parameters are specified on CARDs 3, 3A1 and 3A2 of the tape5-file. There are several options to customize the geometry parameters unambiguously. Based on the available parameters, the

[13] Details on the technical functionality of the parameters can be reviewed in the official manual or – for all parameters actually used in the current model – obtained from the MODTRAN parameter file provided with the data DVD.

line-of-sight geometry was chosen to be computed from the altitude of the sensor (H1), the altitude of the target (H2) and the observation zenith angle (OBSZEN)[14]. MODTRAN computes the solar geometry from the day of the year and the decimal observation time, autonomously. The observation zenith angle corresponds to 180° minus the viewing zenith angle. The satellite's altitude is approximated with ~830 Km, as stated in section 4.3.3. The target's latitude, longitude and altitude are obtained from the initial lake-input-file. At-sensor brightness temperatures were calculated in the spectral range of 10 - 13 μm and at a resolution of 0.01 μm.

When the input file generation has finished, the algorithm starts the IDL-interface MODO, from which MODTRAN is called iteratively. The MODTRAN output is manifold and comprises a full characterization of the simulated atmosphere and the radiation transfer therein. Most important for the subsequent computation of split-window coefficients is the content of the tape5, tape6 and chn-files. The tape5-files remain the same before and after the simulations, hence provide a summary of the input parameters for each model-run. The tape6-files contain log-entries from the simulation and can be particularly helpful for debugging the code. The chn-files contain the AVHRR channel brightness temperatures in the computed spectral range.

4.4 Derivation of split-window coefficients and calculation of LSWTs from AVHRR observations

Step eight of the MODTRAN LSWT algorithm starts with the import of the simulation output from the tape5- and the chn-files. Particularly, this includes reading the brightness temperatures of AVHRR channels 4 and 5 from the chn-file, of the simulation viewing zenith angle, the maximal relative humidity of the underlying ECMWF profile, the total atmospheric water vapor and ozone columns, the wind speed, the simulated skin-temperature and the timestamp of the simulation. In addition the algorithm applies the skin-to-bulk-correction formulated in equation 2.20 (Minnett et al., 2011). The actual derivation of the split-window coefficients is performed by a routine, which implements much of the code provided by Dr. Michael Riffler, for his computations of the RTTOV split-window coefficients. In order to apply this split-window coefficient routine with the MODTRAN data, the MODTRAN output-storage-files were transformed into a RTTOV-matching-format.

[14] A sketch with all available MODTRAN line-of-sight geometry parameters is provided in figure 4 of the MODTRAN FAQ (http://modtran5.com/faqs/index.html).

In step nine of the algorithm, daily split-window coefficients are computed based on a two-stage multi-linear regression with the following modified NLSST equation after Hulley et al. (2011)

$$T_S = a_0 + a_1 \cdot T_4 + a_2 \cdot (T_4 - T_5) + a_3 \cdot (T_4 - T_5) \cdot (1 - sec\theta) \quad (4.1)$$

, where T_S refers to the skin-temperature used in the simulations, a_0 to a_3 represent the split-window coefficients, T_4 and T_5 denote the simulated brightness temperatures of AVHRR channels 4 and 5, respectively, and θ denotes the simulated viewing zenith angle (Hulley et al., 2011). The first multi-linear regression is computed under consideration of at least 15 valid simulations in a 360-day running-window centered at the date of the current iteration, which are limited to observations with VZAs smaller 55°, to physically reasonable brightness temperatures of 268.15 K ≤ $T_{4\,or\,5}$ ≤ 308.15 K for channel 4 and 5, to maximum relative humidities smaller 85% and to differences between the simulated skin-temperature minus the simulated brightness temperature in channel 4 greater 0.5 K. Data points with residuals larger than the residuals' standard deviation of the first fit and greater than a threshold are not considered in the second multi-linear regression. In this way, the second multi-linear regression derives robust estimates for the daily split-window coefficients.. Coefficients are computed per lake (i.e. predefined target pixel) and per satellite, individually. Finally, the split-window coefficients are stored into the IDL-internal save-format in order for them to be available for repeatable usage.

The final step of the MODTRAN LSWT algorithm computes lake surface water temperatures for the specified AVHHR observation corresponding to equation 4.1. The algorithm uses the lake- and satellite-specific split-window coefficients a_0 to a_3, the actually observed AVHRR brightness temperatures T_4 and T_5 and the satellite viewing zenith angle θ to calculate a satellite based LSWT estimate. Similar to the cloud masking procedure, the algorithm extracts 3x3-pixel-patches from the satellite images and distinguishes between land and water with a ratio of channel 2 over channel 1. If at least 2 pixels are identified as water, the procedure obtains the mean LSWT from contributing water pixels and assigns this value to the target pixel. Eight simple quality checks at the end of the computations are implemented for ensuring a certain minimal quality of the final LSWTs, most of them adopted from Kilpatrick et al. (2001). These tests comprise a uniformity (or spatial coherence) test for detection of small cloud contamination, a test for physically reasonable BT4, BT5 and LSWT, a check for suspiciously high reflectance in the NIR (i.e. in channel 2), another test of the channel 2 over channel 1 ratio, but with a stricter rejection threshold of 0.75 than used for the LSWT

computations above, a test against a cutoff angle of 45°[15] and a check of corrupted satellite geometry parameters[16].

For an iterative computation of LSWTs per satellite and target pixel over longer time periods, AVHRR observations were imported satellite-wise and were saved into IDL data array for simple data handling.

[15] The justification for the introduction of a cutoff angle can be found in section 5.1.
[16] Additionally, there is an optional test of the maximal relative humidity against a maximum of 85%, which was not activated for the derivation of the results in chapter 5.

Chapter 5

Results & Discussion

Chapter 5 provides a comparison of the performance of MODTRAN and RTTOV for LSWT retrieval from AVHRR observations. This includes an inspection of the computed brightness temperatures as well as a validation and an analysis of the computed LSWTs against in situ temperatures of three in situ stations at Lake Constance and Lake Geneva. Sources of uncertainties such as large viewing angles, high wind speeds and high relative humidity are evaluated for their impact on the accuracy of simulated LSWTs. Finally, a pixel-wise comparison of Lake Geneva and Lake Constance is used for an indication of distinctive spatial differences between the models.

5.1 Comparison of simulated MODTRAN and RTTOV brightness temperatures

Section 5.1 covers a comparison of the r*aw* simulated brightness temperatures for MODTRAN and RTTOV. In this context *raw* refers to the brightness temperatures of AVHRR channels 4 and 5 obtained from the radiative transfer simulation itself[17]. Thereby this comparison is designed to give first indications on the variability of the models as well as on particular deviations of the models for the different simulation viewing angles.

[17] Notice, that in the following sections brightness temperatures are going to be referred to the brightness temperatures actually acquired by the satellite

Figure 4 shows the simulated NOAA 18 (N18) brightness temperature differences (BTD) between RTTOV and MODTRAN for AVHRR channel 4 (BTD4; top row), channel 5 (BTD5; middle row) and for their difference (BTD45; bottom row) as a function of the viewing zenith angle (VZA) for half a year from December 2007 to May 2008[18]. This includes simulations for the eight simulated VZAs (0°, 15°, 30°, 40°, 45°, 50°, 55°, 60°) and the five skin-temperature-variations proposed by Hulley et al. (2011). The six lakes are color-coded by their in Table 1 defined lake IDs. The two panels in the left column comprise BTDs for VZAs greater or equal 45°, the two panels in the right column show BTDs for VZAs greater 45°. Channel 4 BTDs from 0 to 45° range relatively consistent for all six lakes from –0.8 K to +1.5 K. Offsets from zero-mean are slightly negative for small viewing angles and become positive for VZAs greater 40°. Channel 5 BTDs show slightly larger variability with distributions between -1.5 K and +1.6 K and minor enhanced offsets from zero-mean, but into the same directions as the BTDs of channel 4. The tendency for growing offsets from zero-mean and increasing variability with increasing VZAs becomes considerably more pronounced towards larger viewing angles. For VZAs greater 45° both channels exhibit BTDs an order of magnitude higher than for VZAs less or equal 40° [19]. The distributions for all six lakes show distinct offsets of approx. +1 K for BTDs at 55° and +2 K for BTDs at 60°. The inter-quartile-ranges of the BTD distributions at 60° span ~6 K in the BTD4 plots and ~8 K in the BTD5 plots. Outliers at 60° even approach +10 K. However, since BTDs are of similar magnitude in both channels, these model deviations cancel out in the BTD45 plots (bottom row), where the distributions reach moderate zero-mean offsets of about 0.2 K to -0.3 K and considerably smaller variability, especially at large VZAs (e.g. ~2 K at 60°).

It is evident that MODTRAN and RTTOV perform differently at different VZAs. Compared to RTTOV the MODTRAN atmosphere seems to attenuate radiation substantially stronger at VZAs greater 40°. However, whether RTTOV underestimates the true brightness temperature or MODTRAN overestimates the true brightness temperature is difficult to say at this stage. Reasons for discrepancies between the models can be manifold and would require a much more detailed comparison of the input parameters for *both* models. Hulley et al. (2011) reported incoherent trends for brightness temperatures at large viewing angles for two different lakes and algorithms, as well. In order to minimize the viewing angle effect and achieve high accuracies with their regional approach, they restricted their data set to VZAs of 45°. Because it was observed that the viewing angle effect propagates into the final LSWTs, where it had led to largely incoherent deviations from the validation

[18] The selection of this period is arbitrary.
[19] The scaling of the ordinate differs from panel to panel. In the top and the middle row, the scaling changes by one order of magnitude from the right to the left panel.

data and hence between the models, the suggestion of Hulley et al. (2011) is adapted here as well. This means that satellite observations with VZAs larger than 45° are not considered within the further analysis.

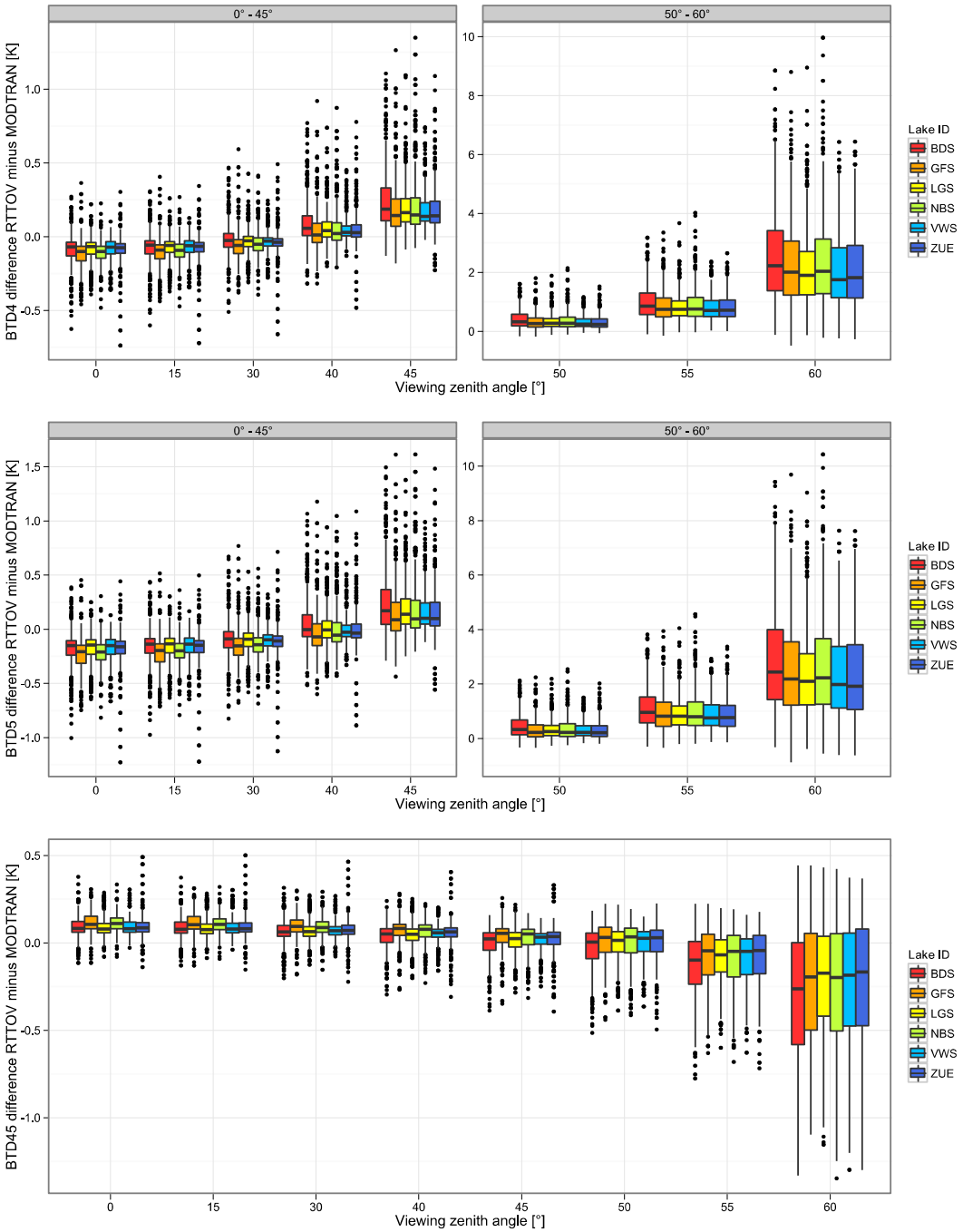

Figure 4: Box-Whisker-Plots for the simulated NOAA18 (N18) RTTOV minus NOAA18 MODTRAN brightness temperature differences of AVHRR channels 4 (BTD4; top row), 5 (BTD5; middle row) and their difference (BTD45; bottom row) as a function of the viewing zenith angle for six large Swiss lakes and for a period between December 2007 and May 2008. Lake IDs refer to Lake Constance (BDS; red), Lake Geneva (GFS; orange), Lake Lugano (LGS; yellow), Lake Neuchâtel (NBS; green), Lake Lucerne (VWS; light-blue) and Lake Zurich (ZUE; dark-blue).

5.2 Comparison of RTTOV and MODTRAN lake surface water temperatures

In the second step of the model analysis, the attention is drawn to the accuracy of the simulated LSWTs when compared to the locally measured in situ surface or near-surface temperatures. In this context, and as already described in section 3.1, a dataset of the in situ water temperature station INRA at Lake Geneva and two datasets of the in situ water temperature stations Brgz and UniK at Lake Constance with a daily or finer temporal resolution are selected for a linear regression analysis. As described in section 4.4, the split-window coefficients were computed individually per model, per satellite and for six Swiss lakes. The in situ periods for the comparison were selected, based on the operational periods of the satellites and on the available periods of the in situ data[20]. In situ data were re-sampled to daily means, in case their temporal resolution outvalues the required daily resolution. The analysis of NOAA17 (N17) data is based on an AVHRR observation period from March 2003 to August 2008. The analysis for NOAA18 data is carried out on an AVHRR observation period from May 2005 to December 2010. Notice that all three in situ stations provide water temperatures acquired in different depths of the epilimnon, namely at the surface (Brgz), in 0.5 m (UniK) and 1.0 m (INRA). Since UniK and Brgz are both representatives for Lake Constance, the LSWT computation for both of them is based on the same set of coefficients.

Figures 5, 6, 7 and 8 visualize the accuracy of the LSWTs as predicted from the model-, lake- and satellite-specific split-window coefficients when compared to the locally measured in situ temperatures at the three in situ temperature stations. In this context, all four figures show scatterplots of simulated LSWTs as a function of in situ water temperatures for the three selected measurement stations INRA, Brgz and UniK (top row), time series of the differences between simulated and in situ water-surface temperatures (middle row) and the corresponding, lake-, model- and satellite-specific split-window coefficients a_0, a_1, a_2 and a_3 according to equation 4.1 (bottom row) per model (MODTRAN, RTTOV) and satellite (N17, N18). The regression models of the scatterplots (top row) are generally of good quality with R-squares above 0.95. Hence, most of the variability in the simulated temperatures can be explained with the in situ temperatures. This supports the overall good agreement of the simulated temperatures with the locally measured temperatures and underpins the capability of the split-window approach, in general. The slopes of the regression lines approximate

[20] An unidentified technical problem with the radiative transfer simulation did not allow coverage of a longer period for NOAA17. A technical problem with the calculation of the brightness temperatures from the satellite-specific spectral response function for NOAA19 and MetOp-A denied an inclusion of those satellites into the comparison.

unity in all cases (i.e. $0.98 \leq \text{slope} \leq 1.08$) and vary only in the decimal digits between MODTRAN and RTTOV for the same in situ station. To some percentage the tilt of the regression line must be attributed to the statistical distributions of the in suit data, which are generally skewed towards higher temperatures. This phenomenon might be of mere technical reasoning, since maintenance of outdoor measurement stations can be significantly more challenging within winter weather conditions and cold temperatures. In situ data gaps are more frequently during winter times. However, due to the very low level of information on the methods of the in situ data sampling, the reason for the skewing of the regression lines remains uninvestigated here.

The intercepts of the linear regression models vary between -1.31 and 0.27, but with an overall tendency towards negative values. Systematic shifts towards negative temperatures do however likely appear for satellite based LSWTs, when validated against in situ temperatures that were not being measured at the actual water surface[21].This is supported by the fact that the smallest offsets as well as the overall best statistics in all four figures come along with water temperatures actually obtained at the water surface, as being the case for the Brgz in situ station at Lake Constance (middle column in figures 5 - 8). The differences between simulated and measured temperatures (middle row) range from -5 to 5 °C. They do not indicate a trend or clearly visible seasonal signal. Apparent abrupt changes in time series of the split-window coefficients do not appear in parallel with periods of larger differences. A seasonal decomposition (results not shown) of the dataset did not show any significant and meaningful seasonal variation. Compared to NOAA17 less data points per in situ station are available for NOAA18. This is on account to the limited availability of continuous in situ measurements over the entire comparison period, and a consequence of the frequency of NOAA17 and NOAA18 overflights per day. While NOAA18 usually passes Central Europe once around midday and once around midnight, N17 passes twice at daytime, once in the morning and once in the evening (Hüsler et al., 2011) . Effectively, N17 is able to deliver a larger amount of valid daytime overpasses.

[21] See section 2.3.3 for a more detailed description of the problem and corresponding references.

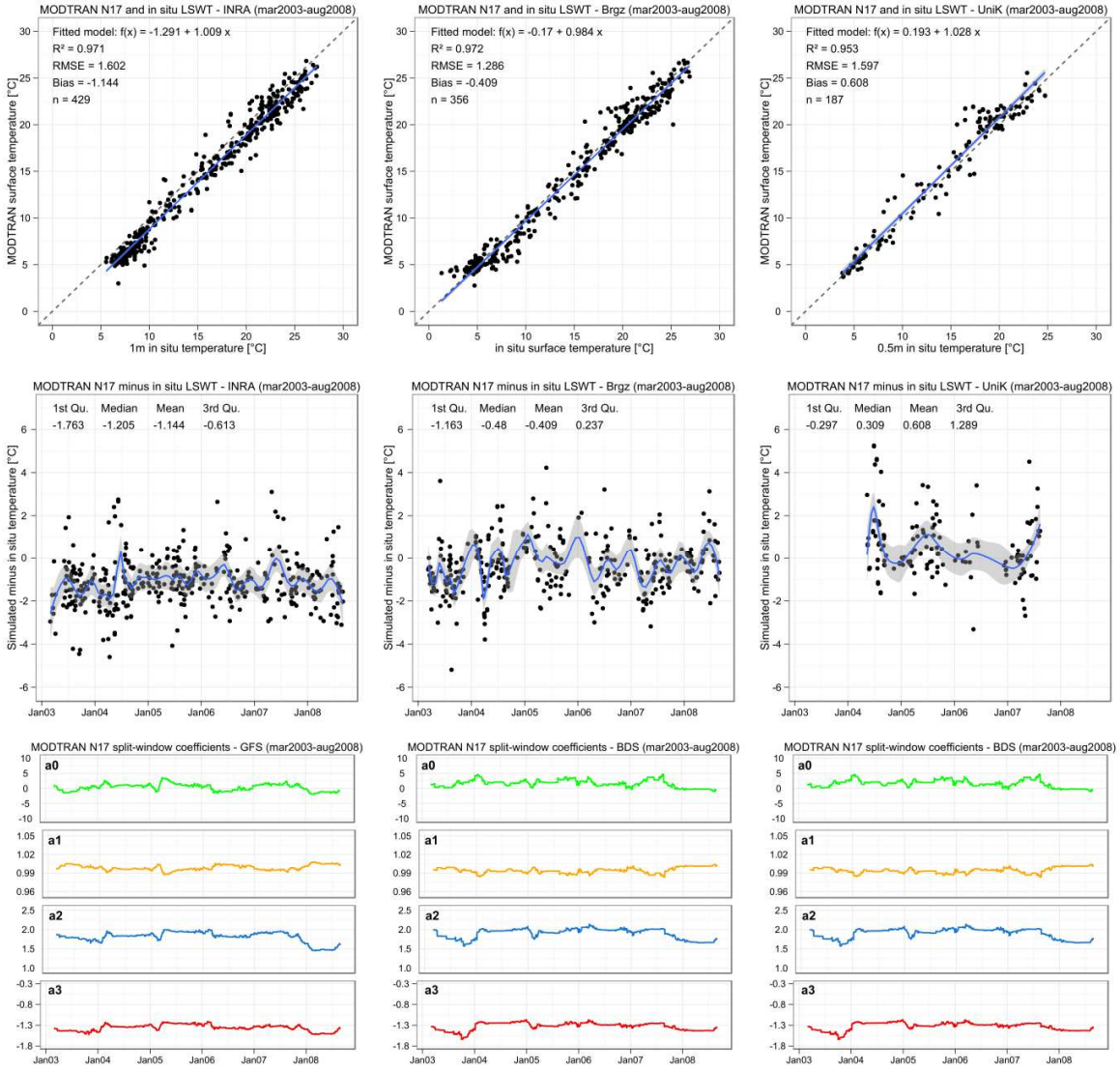

Figure 5: Performance of MODTRAN NOAA 17 (N17) simulated lake surface water temperatures for valid and cloud-free satellite observations against locally measured in situ water temperatures of one fixed station at Lake Geneva (INRA 46.453°N / 6.589°E) and of two fixed stations at Lake Constance (Brgz 47.507°N / 9.748°E; UniK 47.762°N / 9.131°E) for a five-year period from March 2003 to August 2008. The *top row* shows scatterplots and regression statistics for the simulated lake surface temperatures against the measured water surface or near-surface temperatures. The regression line (blue) includes 95% confidence regions (grey shaded). The dashed black line indicates the optimal regression line without bias and with unity slope. The *middle row* visualizes the difference between simulated and measured surface water temperatures. The difference plots are supported with the distribution statistics (i.e. mean, median, 1st and 3rd quartile). The polynomial fit (blue) is obtained from a locally weighted regression with a span of 0.1 (i.e. 10% of the points in the vicinity are used for the fit) and displayed with a 95%-confidence region (grey shaded). The *bottom row* displays the four lake- and model-specific split-window coefficients a_0 (green), a_1 (orange), a_2 (blue) and a_3 (red) for the period of consideration, whereas GFS denotes Lake Geneva and BDS denotes Lake Constance. *Remark: The split-window coefficients for Brgz and UniK are identical.*

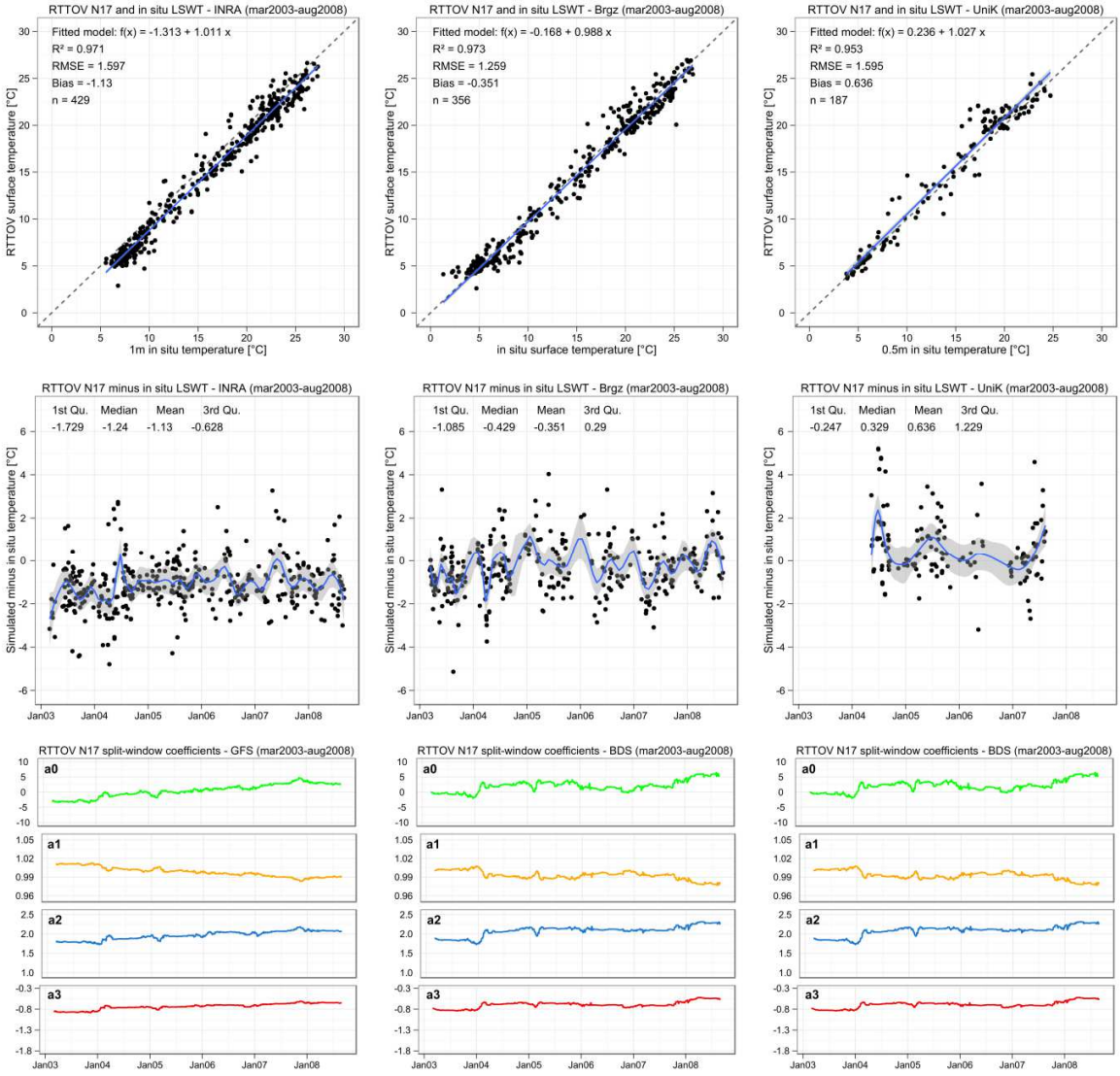

Figure 6: Performance of RTTOV NOAA 17 (N17) simulated lake surface water temperatures for valid and cloud-free satellite observations against locally measured in situ water temperatures at one fixed station at Lake Geneva (INRA 46.453°N / 6.589°E) and two fixed stations at Lake Constance (Brgz 47.507°N / 9.748°E; UniK 47.762°N / 9.131°E) for a five-year period from March 2003 to August 2008. The *top row* shows scatterplots and regression statistics for the simulated lake surface temperatures against the measured water surface or near-surface temperatures. The regression line (blue) includes 95% confidence regions (grey shaded). The dashed black line indicates the optimal regression line without bias and with unity slope. The *middle row* visualizes the difference between simulated and measured surface water temperatures. The difference plots are supported with the distribution statistics (i.e. mean, median, 1st and 3rd quartile). The polynomial fit (blue) is obtained from a locally weighted regression with a span of 0.1 (i.e. 10% of the points in the vicinity are used for the fit) and displayed with a 95%-confidence region (grey shaded). The *bottom row* displays the four lake- and model-specific split-window coefficients a_0 (green), a_1 (orange), a_2 (blue) and a_3 (red) for the period of consideration, whereas GFS denotes Lake Geneva and BDS denotes Lake Constance. *Remark: The split-window coefficients for Brgz and UniK are identical.*

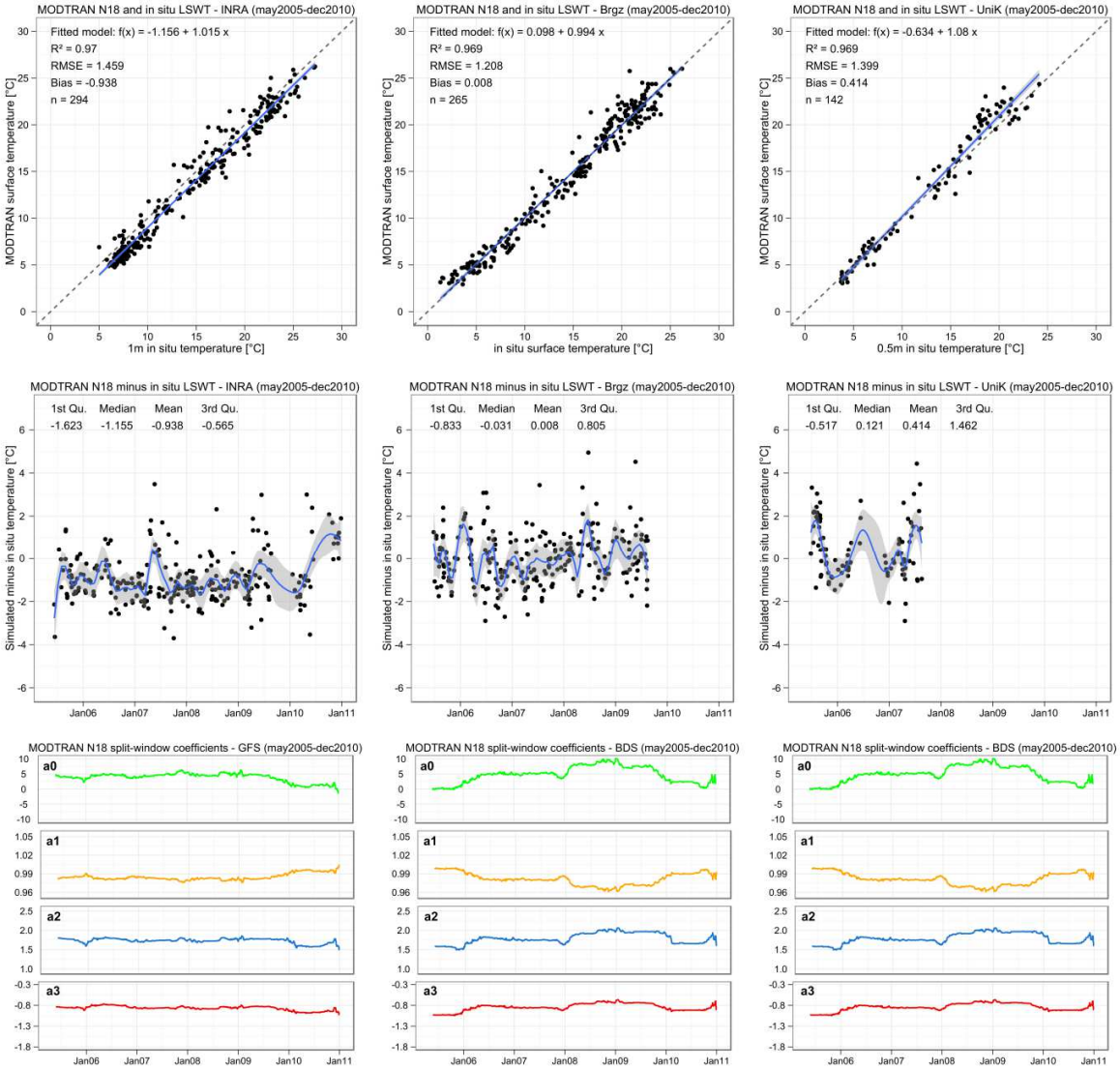

Figure 7: Performance of MODTRAN NOAA 18 (N18) simulated lake surface water temperatures for valid and cloud-free satellite observations against locally measured in situ water temperatures at one fixed station at Lake Geneva (INRA 46.453°N / 6.589°E) and two fixed stations at Lake Constance (Brgz 47.507°N / 9.748°E; UniK 47.762°N / 9.131°E) for a five-year period from May 2005 to December 2010. The *top row* shows scatterplots and regression statistics for the simulated lake surface temperatures against the measured water surface or near-surface temperatures. The regression line (blue) includes 95% confidence regions (grey shaded). The dashed black line indicates the optimal regression line without bias and with unity slope. The *middle row* visualizes the difference between simulated and measured surface water temperatures. The difference plots are supported with the distribution statistics (i.e. mean, median, 1st and 3rd quartile). The polynomial fit (blue) is obtained from a locally weighted regression with a span of 0.1 (i.e. 10% of the points in the vicinity are used for the fit) and displayed with a 95%-confidence region (grey shaded). The *bottom row* displays the four lake- and model-specific split-window coefficients a_0 (green), a_1 (orange), a_2 (blue) and a_3 (red) for the period of consideration, whereas GFS denotes Lake Geneva and BDS denotes Lake Constance. *Remark: The split-window coefficients for Brgz and UniK are identical.*

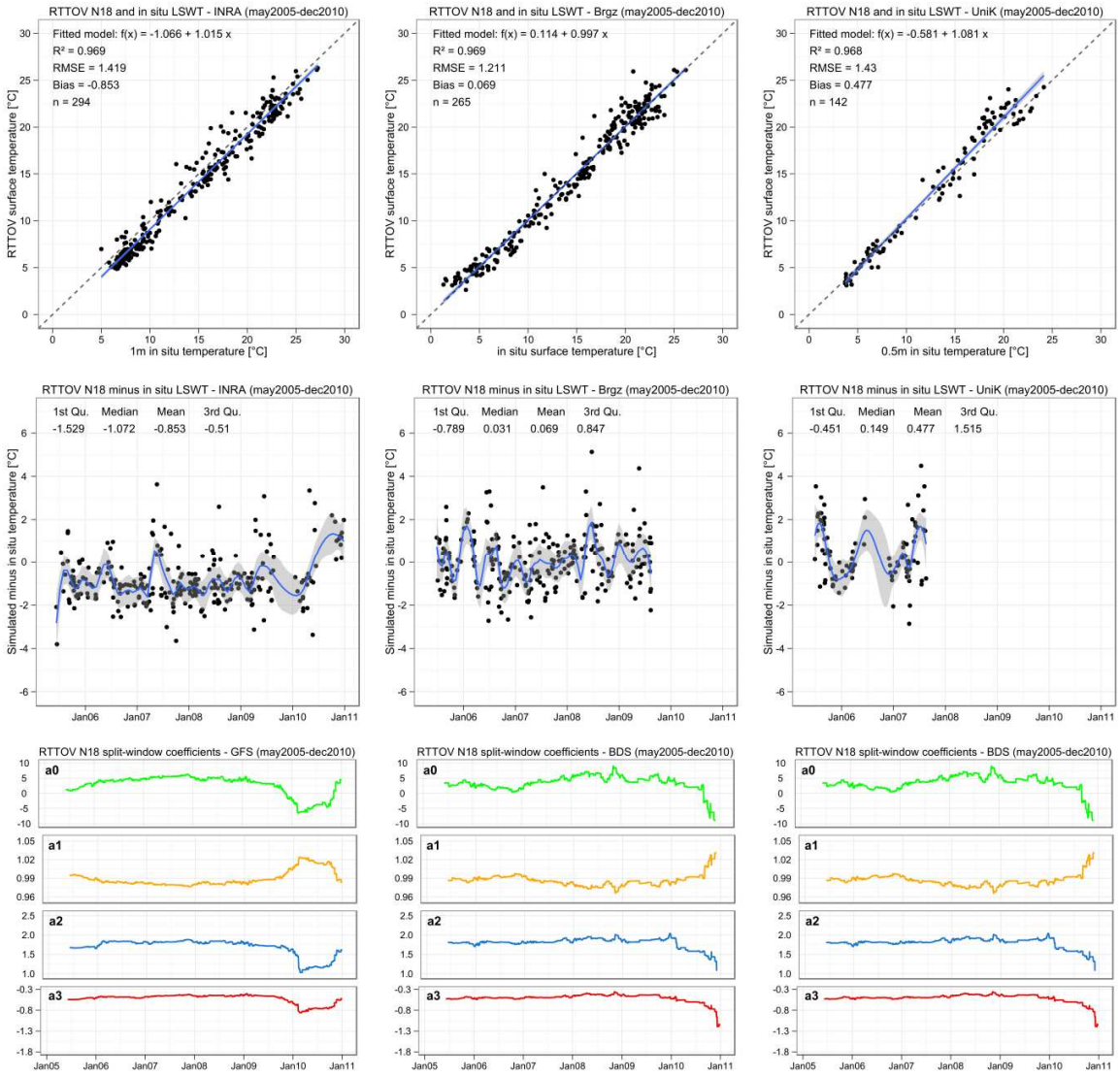

Figure 8: Performance of RTTOV NOAA 18 (N18) simulated lake surface water temperatures for valid and cloud-free satellite observations against locally measured in situ water temperatures at one fixed station at Lake Geneva (INRA 46.453°N / 6.589°E) and two fixed stations at Lake Constance (Brgz 47.507°N / 9.748°E; UniK 47.762°N / 9.131°E) for a five-year period from May 2005 to December 2010. The *top row* shows scatterplots and regression statistics for the simulated lake surface temperatures against the measured water surface or near-surface temperatures. The regression line (blue) includes 95% confidence regions (grey shaded). The dashed black line indicates the optimal regression line without bias and with unity slope. The *middle row* visualizes the difference between simulated and measured surface water temperatures. The difference plots are supported with the distribution statistics (i.e. mean, median, 1st and 3rd quartile). The polynomial fit (blue) is obtained from a locally weighted regression with a span of 0.1 (i.e. 10% of the points in the vicinity are used for the fit) and displayed with a 95%-confidence region (grey shaded). The *bottom row* displays the four lake- and model-specific split-window coefficients a_0 (green), a_1 (orange), a_2 (blue) and a_3 (red) for the period of consideration, whereas GFS denotes Lake Geneva and BDS denotes Lake Constance. *Remark: The split-window coefficients for Brgz and UniK are identical.*

Overall, similarities are strong between the radiative transfer models MODTRAN and RTTOV. For the individual stations and satellites, neither scatterplots or -statistics nor difference-plots or -statistics seem to differ in a distinct manner, although the course of the split-window coefficients per model, per satellite and per lake varies individually over time, most notable for coefficients a_0 and a_3. From the coefficient differences of RTTOV minus MODTRAN (see Appendix C) it becomes apparent that the variability of the coefficients a_0, a_1 and a_2 fluctuates around zero incoherently. The viewing-angle-dependent coefficient a_3 shows a relatively consistent positive bias for all lakes. This could however been expected, since coefficient a_3 inherits the brightness temperature difference of channel 4 and 5 as well as the viewing zenith angle.

Regardless of the consistent bias for $a_{3,}$ the concurrence in the model accuracy is undeniable. This fact is additionally supported by Figure 9, which shows the Box-Whisker-Plots (upper panel) and the density distribution functions (upper panel) for the differences of simulated minus locally measured temperatures per in situ temperature station and satellite. There is a strong agreement of the density curves and Bow-Whisker-Plots for both models.

It should be noted, that only the density distribution for the Brgz station can clearly be assumed to obey the central limit theorem and thus originate from a Gaussian distribution. Particularly, the density shapes of the N18 INRA and the N18 UniK data seem to possess a minor secondary peak in the range between 0.5 °C and 2 °C. A possible reason could be the skin-effect in combination with the relatively regular overpasses of the satellites at specific daytimes. The skin effect is able to impose a positive offset to the satellite temperature measured at the surface against the in situ temperature measured at 1m depth, especially in the diurnal course of a warm summer day (c.f. figure 1 and 2 in Donlon et al. (2002), which in turn can yield a systematic shift in the density distribution of the differences for summer temperatures, finally notable as a secondary peak. Further investigations with a particular focus on the diurnal and seasonal structure of simulated LSWTs would have to verify this assumption. Since this secondary-peak appears for RTTOV and MODTRAN concurrently, it can be assumed that it does not trigger major differences between the models.

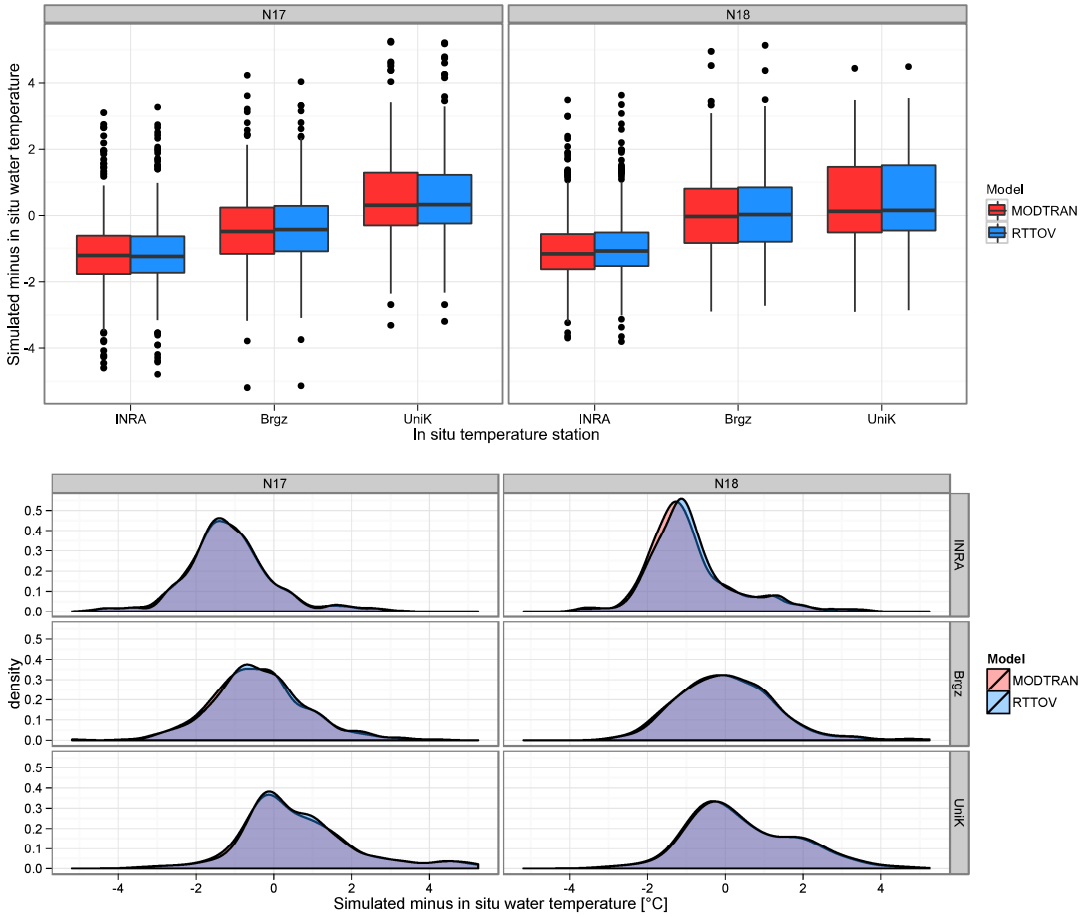

Figure 9: Statistical distributions and Box-Whisker-Plots of the differences between locally measured and simulated temperatures per satellite (N17, N18), in situ temperature stations (INRA 46.453°N / 6.589°E; Brgz 47.507°N / 9.748°E; UniK 47.762°N / 9.131°E) and radiative transfer model (MODTRAN, RTTOV).

A full test-based comparison of the means, variances, errors and coefficients has been considered to be inappropriate for an investigation of the different performance of the two models in a practical sense. Even though paired and unpaired Student's t-test and Wilcoxon singed-rank-tests were performed (data not shown), they solely helped to identify the existence of a difference between the models, which could not be inferred from a visual inspection of the statistics and plots of figures 5 to 9. However, since the magnitude of the variance can be attributed to lie in the order of the acquisition error[22], the knowledge about a statistically verified existence of a minor model difference is of inferior importance. Thus it was decided to perform the analysis of accuracy in terms of the root mean square error (RMSE) and the bias after Hulley et al. (2011). The RMSE represents a widely used

[22] Hulley et al. (2011) incorporated noise-equivalent differential temperatures (NEΔT) of ~0.5 K for AVHRR/3. Trishchenko et al. (2002) attributed noise-equivalent differential temperatures of ~0.12 K to AVHRR/3 on the NOAA15 and NOAA16 platforms.

parameter for the assessment of variability in model comparisons, is relatively sensitive to large errors and is expressed in the same unit as the variable of consideration (Willmott & Matsuura, 2005).

Table 4 summarizes the linear regression statistics of figure 5, 6, 7 and 8 including RMSEs and biases. The weighted arithmetic means were computed from a summation of the multiplied lake-specific statistical parameters by its corresponding observation number n, and subsequent division by the total amount of satellite observations. This procedure is considered to give a better indication of the overall performance than a recalculation of the regression parameters with pooled datasets[23]. The weighted mean RMSEs indicate model variances of ~0.01 K for NOAA17 and NOAA18, likewise. Weighted mean biases differ by about ~0.07 K. Again, these variances range among acquisition errors and should not lead to any final conclusion about the model performance.

Table 4: Summary of the linear regression statistics of Figure 5, 6, 7 and 8. The weighted mean was computed as the average per statistical parameter over all lakes, weighted by the number of available data points n.

		MODTRAN				**RTTOV**			
		INRA	Brgz	UniK	*Weighted arithmetic mean*	INRA	Brgz	UniK	*Weighted arithmetic mean*
NOAA 17	Slope	1,009	0,984	1,028	*1,003*	1,011	0,988	1,027	*1,006*
	Intercept	-1,291	-0,170	0,193	*-0,595*	-1,313	-0,168	0,236	*-0,596*
	R^2	0,971	0,972	0,953	*0,968*	0,971	0,973	0,953	*0,968*
	RMSE	1,602	1,286	1,597	*1,485*	1,597	1,259	1,595	*1,473*
	Bias	-1,144	-0,409	0,608	*-0,538*	-1,130	-0,351	0,636	*-0,505*
	n	429	356	187		429	356	187	
NOAA 18	Slope	1,015	0,994	1,080	*1,020*	1,015	0,997	1,081	*1,022*
	Intercept	-1,156	0,098	-0,634	*-0,576*	-1,066	0,114	-0,581	*-0,522*
	R^2	0,970	0,969	0,969	*0,969*	0,969	0,969	0,968	*0,969*
	RMSE	1,459	1,208	1,399	*1,352*	1,419	1,211	1,430	*1,343*
	Bias	-0,938	0,008	0,414	*-0,307*	-0,853	0,069	0,477	*-0,235*
	n	294	265	142		294	265	142	

In the next section the differences between modeled and measured LSWTs are investigated for their dependencies on parameters that are able to violate the assumptions in the split-window method.

[23] Reasons lie in the different biases for the individual lake regression lines due to the variant measurement depths, and in the inconsistent number of observations n.

5.3 Analysis of influencing factors on the model performances

In order to inspect the robustness of the simulated LSWTs for RTTOV and MODTRAN, this section dwells on the variability of simulated LSWTs with the water vapor profile, the surface emissivity and the atmospheric optical path. In particular, this involves investigations of the simulation errors (i.e. simulated minus in situ LSWT) against the maximum relative humidity, the wind speed and the viewing zenith angle.

Figure 10 shows the simulated MODTRAN and RTTOV LSWTs minus the in situ temperatures as a function of the zenith viewing angles of the corresponding satellite measurements for N17 and N18. Within a total range of -5 to 5 °C, temperature differences appear invariant with view angle. The differences in brightness temperatures for different VZAs that have been encountered in section 5.1, seem to can hardly be traced in the final simulated LSWT errors.

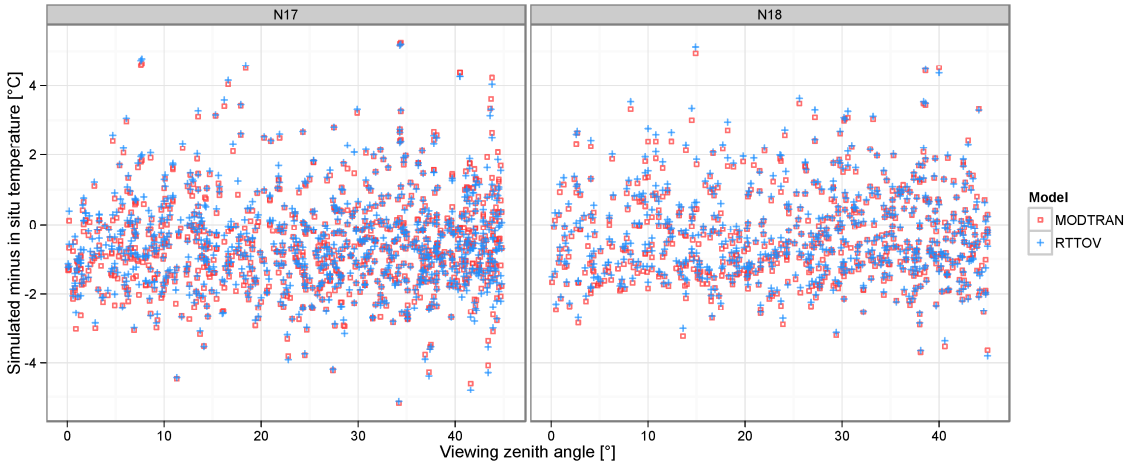

Figure 10: Differences between simulated lake surface water temperatures and in situ temperatures as a function of the viewing zenith angle.

Figure 11 shows the MODTRAN and RTTOV LSWTs minus the in situ temperature differences as a function of the maximal relative humidity of the underlying ECMWF profile (upper panel) and of the wind speed (lower panel) for N17 and N18. There is no indication for a dependency of the simulation errors on the maximal relative humidity of the underlying climatology. The data show homogenous point clouds for both models. A similar invariance holds for the simulation errors when plotted as a function of wind speed. Both models show an apparent robustness against singular large wind speeds and large amounts of water vapor, which supports the quality of the modeling approach undertaken in this study and underpins the equal sophisticated level of the radiative transfer models in use.

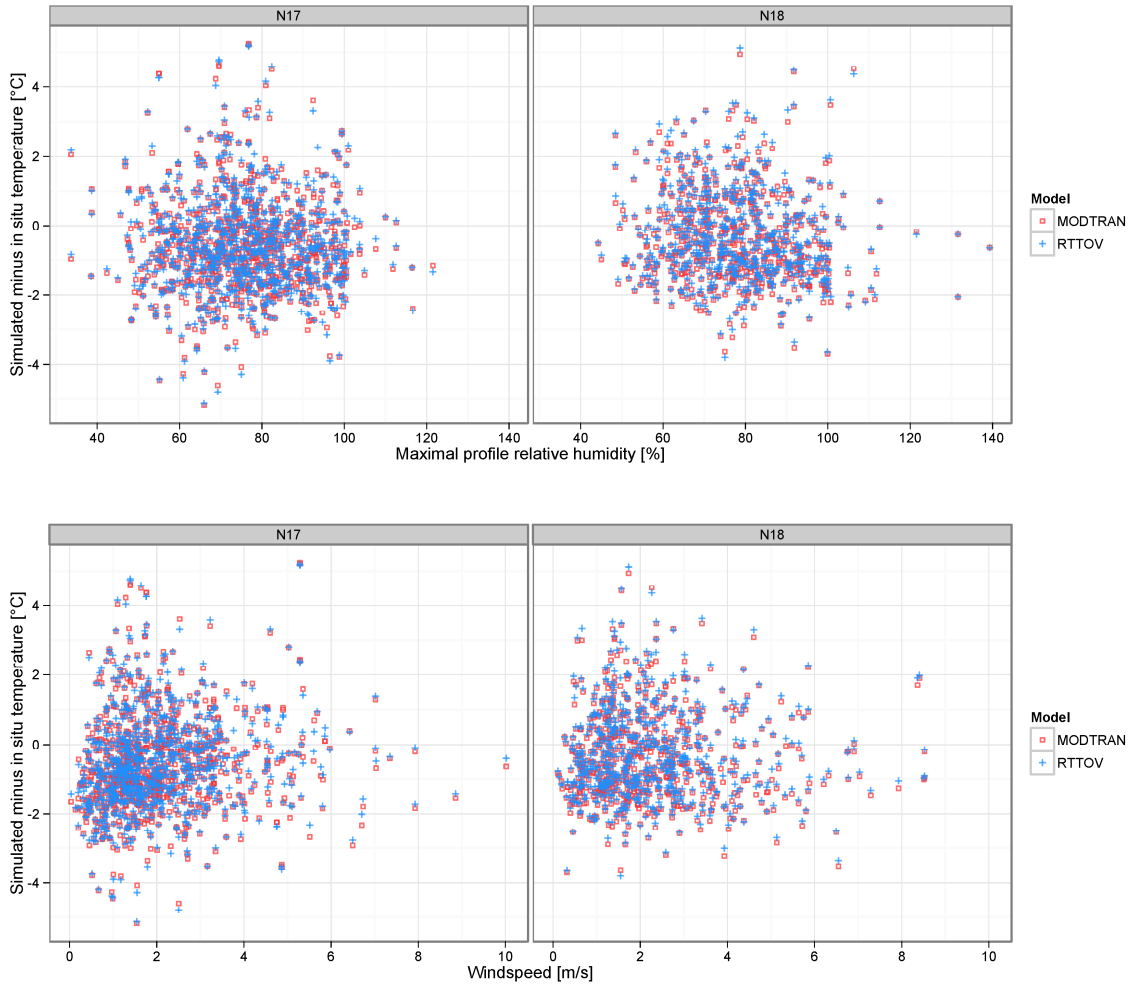

Figure 11: Simulated minus in situ water surface temperatures for MODTRAN and RTTOV as function of the maximum profile relative humidity (top panel) and wind speed (bottom panel).

5.4 Spatial comparison of RTTOV and MODTRAN lake surface water temperatures

By now the differences in the RTTOV and the MODTRAN radiative transfer simulations have been examined as the difference between the actually measured and the simulated LSWTs of one single validation pixel. In section 5.4, the model differences are accessed directly by a subtraction of the simulated LSWTs for two clear sky satellite scenes in April 2007 as being computed not only for one target pixel, but for the entire target lake. For matters of consistency this investigation remains focused on Lake Constance and Lake Geneva.

Figure 12 shows the differences in RTTOV minus MODTRAN LSWTs for Lake Constance and Lake Geneva. The displayed regions cover areas from 47.9°N / 8.9°E to 47.4°N / 9.8°E in panel (a) and (c) and from 46.6°N / 6.05°E to 46.2°N / 7.05°E in panel (b) and (d). One pixel represents an area of 1.1 km² and corresponds to the spatial resolution of the AVHRR/3 sensor. Land pixels were masked with the Channel 2 over Channel 1 ratio, which is described in the LSWT post-quality assessment (see section 4.4), against a rather strict cutoff-threshold of 0.75. A positive consequence of this strict threshold becomes apparent from the small amount of highly biased shoreline pixels, which were being flagged incase the risk of land contamination was higher than allowed by the threshold. In exchange, only few pixels from the narrow, north-eastern parts of Lake Constance (Lake Überlingen and Lake Radolfzell) are displayed. The mean, standard deviation and number of water pixels per lake are given within the corresponding panels.

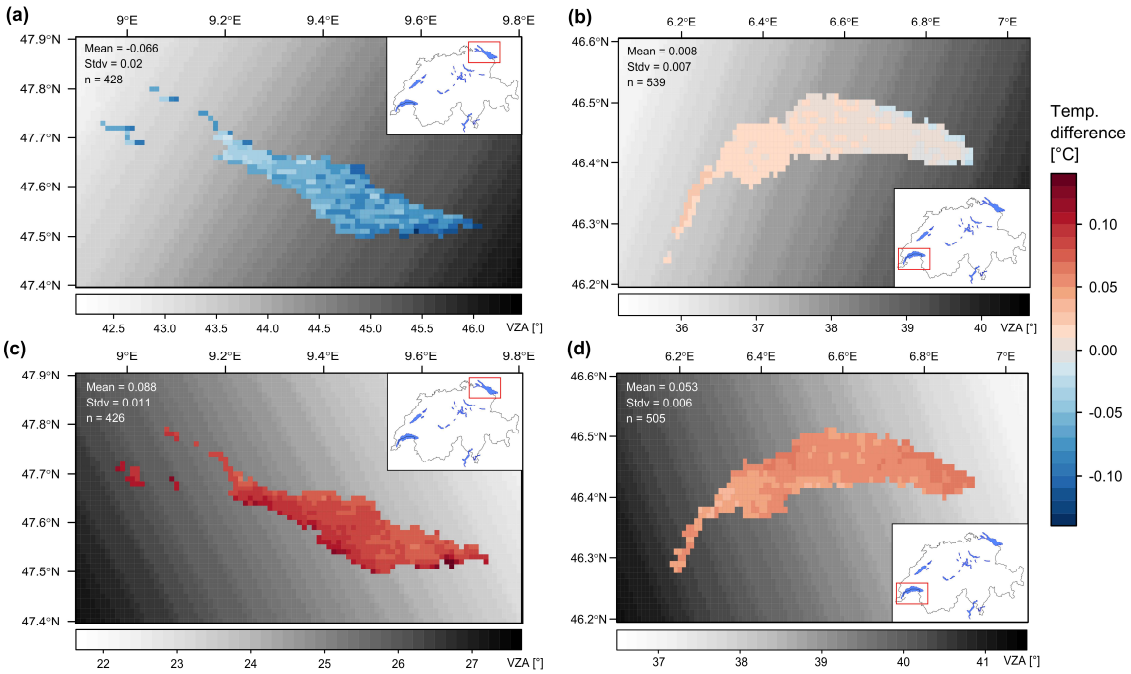

Figure 12: Plots of Lake Constance [(a) and (c)] and Lake Geneva [(b) and (d)] with the pixel-wise differences of simulated RTTOV minus MODTRAN lake-surface water temperatures and the viewing zenith angle (VZA) for two AVHRR subsets in April 2007. Panels (a) and (b) are computed from a NOAA 17 observation of April 10th, 2007 at 10:50 UTC. Panels (c) and (d) are computed from a NOAA 18 observation of April 16th, 2007 at 12:02 UTC. The subsets correspond to areas from 47.9°N / 8.9°E to 47.4°N / 9.8°E in panels (a) and (b) and from 46.6°N / 6.05°E to 46.2°N / 7.05°E in panel (b) and (d). One pixel represents the area of a 1-km²-area, i.e. the spatial resolution of the AVHRR-3 sensor. The spatial standard deviation (Stdv), the spatial mean (Mean) and the number of valid water pixels per plot (n) are indicated in the upper left corner of each panel. *Remark: The scales of the viewing zenith angles (VZA) differ from panel to panel.*

RTTOV minus MODTRAN LSWT differences range from approximately 0.0 K to -0.14 K with total bias of -0.066 K on April 10th, 2007 and from approximately ~0.5 K to 0.14 K with a total bias of +0.088 K on April 16th, 2007 for Lake Constance. For Lake Geneva the LSWT variability is generally lower and shows only on April 16th, 2007 a distinct difference from zero bias (~0.053 K). Overall, the models perform with less variability for Lake Geneva. Shoreline-pixels tend to show the "largest" deviations. This could be expected, since both models use the same split-window linear regression method optimized for surface water temperature retrieval. When the probability for pixel-land-contamination raises (as it is the case for shoreline-pixels), so that the surroundings of the model assumptions are violated, divergence in the simulated LSWTs become likely. Without any technical investigations this can be inferred from the sensitivity of the split-window technique to channel 4 and 5 brightness temperatures, which can be distinctly different for land and water pixels. Although overall gradients of less than 0.1 °C are almost too small for any reliable statistical inference, one could argue about a dependency of the LSWT differences on the viewing zenith angle (VZA). Panel (a), (b) and (d) show an anti-proportional relation for LSWT differences against growing VZAs. LSWT differences decrease with growing VZSs. Lake Constance on panel (c) does however indicate a comparably "strong" reversed behavior for growing VZAs. Overall, this dependence is considered to be of minor importance. An investigation on the temporal development of the kernel with methods from spatial statistics might give additional insight, whether there is a VZA-dependency present in the data.

Overall, the spatial deviations between the models are small and lie within the data acquisition errors. The findings confirm the results discussed in the previous sections of chapter 5.

5.5 Summary of results and general discussion

Both models, MODTRAN and RTTOV, have shown to deliver split-window coefficients derived LSWTs with promising accuracies for Lake Constance and Lake Geneva. The accuracy of both models is attributed with approximately 1.5°C, which is, however, not representative for the achievable accuracy that could be accomplished with an elaborated quality assessment (cf. Kilpatrick et al., 2001; Hulley et al., 2011). In the framework of this study only basic quality checks have been implemented in order to verify the validity of the results in a general sense. The best overall results were detected if the simulated LSWTs are compared to actual surface-water in situ temperatures. Validations of simulated LSWTs to "bulk" in situ water-temperatures showed larger biases. This was expected and can be reliably attributed to the diurnal skin-effect, which is well-known and

documented in the literature (e.g. Donlon et al., 2002, 2007; Gentemann et al., 2003; Minnett et al., 2011). The calculated statistical parameters only deviate in the decimals for simulated RTTOV and simulated MODTRAN LSWTs per lake and satellite. Weighted NOAA17 and NOAA18 averages of those parameters indicate a fairly better performance of RTTOV in terms of smaller RMSEs (~0.01 K) and smaller baises (~0.07 K).

As has been shown in section 5.1, simulated MODTRAN and RTTOV brightness temperatures for channel 4 and 5 distinctly diverge with growing viewing zenith angles. This divergence is strongly mediated in the channel BT differences, because the deviations increase with the same magnitude and into the same direction for both channel 4 and 5 in parallel. The split-window multi-linear regression has shown to be robust against such BT deviations, considering that a consistent divergence of the models into one direction could not be traced in the final LSWTs anymore. This result is rather unrewarding, because it makes the detection of errors that arise from BT differences, as well as an appropriate decoupling of these errors a challenging issue. The equalization of the model differences by the subtraction of BTs in channel 4 and 5 is considered to be the main reason for the invariance of the individual signatures of MODTRAN and RTTOV in the final LSWTs.

The spatial comparison (see section 5.4) depicts an approach to visualize model differences that had not been detected with the single-pixel-comparison of the previous sections. In this context, two cloud-free satellite scenes of April 2007 were selected for the calculation of a pixel-wise difference map of RTTOV minus MODTRAN LSWTs. Once again, the results only indicated small deviations for the models for data of Lake Constance and Lake Geneva. A visual inspection of the LSWT variability as a function of VZAs for the same lakes did show inconsistent trends for different sub-scenes, hence allow no unambiguous conclusion. Apparently, the lack of spatially covering in situ data does not allow an extensive examination of spatial differences against a validation source.

As reported by Hulley et al. (2011), one problem for regional LSWT studies of this kind remains the availability of reliable validation data sets from in situ lake water temperature measurements. Most of the collected in situ datasets for this study provide temporal resolutions of one measurement per month at one specific lake location. Although measurement periods might reach back into to the start-up of the AVHRR observation period, available in situ data coinciding with cloud free satellite observations are of very limited occurrence. Continuously measure in situ data from fixed measurement stations have shown to be a very viable source for validation data. However, measurement stations close to the shoreline are likely to be contaminated with land pixels in the satellite observations and therefore obey the mixed-pixel-problem. This problem also becomes

apparent from Figure 12, where the largest LSWT differences become visible in the vicinity of the Brgz in situ station at the south-eastern shore of Lake Constance (compare with Figure 1).

All results point into the same direction, indicating that the performance of RTTOV and MODTRAN is similar in the context of regional LSWT derivation with the split-window technique. Even though RTTOV yielded fairly better averaged RMSEs and biases (see Table 4), the encountered differences are very small. Accordingly, the question arises, whether the criteria for a decision-making should be reweighted and/or reconsidered. Criteria in this concern could consist of economic reasoning (e.g. software license fees, know-how) or of other performance parameters than mere accuracy (e.g. simplicity, computation speed). It has to be noted that some of these criteria had already determined the decision for choosing RTTOV over MODTRAN in the first place – at that time, when the realization of an operational algorithm was in a planning stage at the RSGB. Because the RTTOV LSWT algorithm can be considered to work faster, simpler and less computing-power-intensive, a MODTRAN LSWT algorithm would have to show conspicuously higher accuracies in order to justify a model exchange at the present stage, where the RTTOV algorithm is fully implemented and validated. With a sufficient expertise a parallel implementation of a MODTRAN algorithm might however be viable, since MODTRAN still offers a variety of functions for adjustment and tuning, which could not be evaluated in the framework of this study.

According to section 2.3.3, there are other named and unnamed sources of uncertainty that could not be explicitly reviewed and examined in the framework of this study. In particular, this corresponds to low level fog, sub-pixel clouds and cloud shadowing, which would not be filtered with the rather simple quality check applied here. A sophisticated post-processing quality management that is tuned to regional climatic phenomena might be a powerful mechanism to screen uncertainties of this kind. Although the absence of such a screening mechanism contributes to a minor accuracy of the simulated LSWTs in total, it is assumed that both models, RTTOV and MODTRAN, obey the introduction of such uncertainties to the same extend. Hence, it is likely that a sophisticated post-processing quality check would reduce the accuracy differences of the models even further.

Chapter 6

Conclusion & Outlook

In the framework of global climate change, alterations of lake ecosystems and their catchments can have serious implications for humans, animals and plants. Lake water temperature has shown to constitute one key factor for obtaining systematic shifts within such ecosystems. In this context, the assessment of lake surface water temperatures (LSWT) with modern space-borne remote sensing techniques is capable of delivering lake covering temperature data sets, which can provide a viable complementary data archive for investigations on regional climate change over the past decades. The AVHRR instrument is one representative from the variety of sensors mounted on satellite platforms, whose first observations date back to the end of the 1970s. The Remote Sensing Group Bern (RSGB) extensively collected AVHRR observations over the European Area and now possesses a continuously growing archive, available for multiple purposes and enquires.

This study utilized a recently published algorithm of Hulley et al. (2011) for LSWT retrieval from inland water bodies in combination with the MODTRAN radiative transfer model in order to derive LSWTs for Swiss lakes from the AVHRR archive of the RSGB. The model performance was evaluated in terms of the accuracy against locally measured water temperatures and compared to the accuracy of a reference algorithm that implements the RTTOV radiative transfer model. The comparison of the simulated LSWTs is carried out on three selected in situ data sets of Lake Constance and Lake Geneva from a larger in situ data archive, which was collected from several Swiss, French and Austrian administration offices and scientific institutions in the framework of this study.

The results indicate a good performance of the RTTOV algorithm and the MODTRAN algorithm, with slightly smaller satellite-averaged root mean square errors and biases for the RTTOV model. A comparison of the raw simulated brightness temperature outputs for AVHRR channels 4 and 5 indicated a growing divergence for large viewing zenith angles above 40° and a general dependency of at least one of the models on this parameter. This divergence could however not been detected in the final LSWTs anymore. An investigation of the simulated LSWT sensitivities against wind speed, viewing angle and maximal relative humidity showed relative invariances for both models. A spatial comparison of LSWTs for Lake Geneva and Lake Constance supported the hypothesis that MODTRAN and RTTOV perform similarly, with final differences of LSWTs in the order of the data acquisition error and below. Based on the results obtained from the investigations above, other economic or scientific criteria would have to be considered within the decision-making for one model or the other. However, since the RTTOV algorithm is fully implemented, validated and operational at the Geographical Institute of Bern, a MODTRAN-based alternative would have to show a conspicuously better performance in terms of accuracy than the fast and accurate working RTTOV code. With the approach and the parameters sets used in this study this goal could not be achieved.

At this point further investigations could focus on the discrepancies that have been encountered during this study. Although, changes in the models where not apparent in the single target-pixel-comparison a spatial comparison with the skin temperatures provided by the ECWMF database could be estimated to giving some insight into the spatial accuracy of the models. Additionally, a full implementation of the Masuda emissivity model (Masuda, 2006) might yield a performance enhancement for the MODTRAN algorithm. For regional studies, it is also imaginable that the split-window approach proposed by Hulley et al. (2011) could be tuned with additional regression coefficients in order to capture and represent emerging tropospheric disturbances, such as Saharan dust events or volcanic eruptions. This would involve detailed investigation on the deviations between simulated and in situ measured LSWT under consideration of the causing event itself. As has been described, water stratification in Swiss lakes can be of complex nature. A correction of the skin-effect in epilimnic water layers for a range of typical surface-near measurement depths would greatly help to incorporate more data into the validation procedure. A review of in situ data measured in different surface-near depths and calculating regression statistics against satellite data could help to develop depth-dependent corrections for inland water bodies. The linear regression statistics derived for the in situ stations in 0.5 m and 1.0m depths might give an indication of the general magnitude of an offset that would have to be expected for simulated LSWTs validations in the European alpine region.

The split-window approach in combination with radiative transfer simulations has generally confirmed its viability for assessing lake surface water temperatures. Thereby, the modern elaborated radiative transfer codes RTTOV and MODTRAN have shown to achieve similar accuracies. In the same context, AVHRR observations have reaffirmed their potential for spatially covering long-time series water temperature measurements. In combination with sophisticated lake stratification models, such as presented by Peeters et al. (2002), space-borne water temperature measurements could greatly help to describe lake ecosystems and their responses to regional and global climate change.

References

Adrian, R., Reilly, C. M. O., Zagarese, H., Baines, S. B., Dag, O., Keller, W., Livingstone, D. M., et al. (2010). UKPMC Funders Group Lakes as sentinels of climate change. *Science And Technology*, *54*(6), 2283–2297.

Anding, D., & Kauth, R. (1970). Estimation of sea surface temperature from space. *Remote Sensing of Environment*, *1*(4), 217–220. doi:10.1016/S0034-4257(70)80002-5

Austin, J. A., & Colman, S. M. (2007). Lake Superior summer water temperatures are increasing more rapidly than regional air temperatures: A positive ice-albedo feedback. *Geophysical Research Letters*, *34*(6), 1–5. doi:10.1029/2006GL029021

Barton, I. J. (1983). Dual channel satellite measurements of sea surface temperature. *Quarterly Journal of the Royal Meteorological Society*, *109*(460), 365–378. doi:10.1002/qj.49710946009

Barton, I. J. (1995). Satellite-derived sea surface temperatures: Current status. *Journal of Geophysical Research*, *100*(95), 8777–8790.

Berk, A., Anderson, G. P., Acharya, P. K., & Shettle, E. P. (2008). *MODTRAN 5.2.0.0 User's Manual* (p. 107). Spectral Science, Inc.; Air Force Research Laboratory; Naval Research Laboratory.

Berk, A., Berstein, L. S., Adler-Golden, S. M., & Lockwood, R. B. (2005). MODTRAN5: A reformulated atmospheric band model with auxiliary species and practical multiple scattering options. (A. M. Larar, M. Suzuki, & Q. Tong, Eds.)*SPIE Proceeding, Multispectral and Hyperspectral Remote Sensing Instruments and Applications II*, *5655*, 88–95. doi:10.1117/12.578758

Bindoff, N. L., Willebrand, J., Artale, V., Cazenave, A., Gregory, J. M., Gulev, S., Hanawa, K., et al. (2007). Chapter 5: observations: oceanic climate change and sea level. In S. Solomon, D. Qin, M. Manning, Z. Chen, M. Marquis, K. B. Averyt, M. Tignor, et al. (Eds.), *Climate Change 2007: The Physical Science Basis. Contribution of Working Group I to the Fourth Assessment*

Report of the Intergovernmental Panel on Climate Change (pp. 385–432). Cambridge, United Kingdom and New York, NY, USA: Cambridge University Press.

Brown, O. B., & Minnett, P. J. (1999). *MODIS Infrared Sea Surface Temperature Algorithm - Algorithm Theoretical Basis Document (Version 2.0). Time* (p. 98). Miami: University of Miami, FL (USA).

Casey, K. S., Brandon, T. B., Cornillon, P., Evans, R., Barale, V., Gower, J. F. R., & Alberotanza, L. (2010). The Past, Present, and Future of the AVHRR Pathfinder SST Program. In V. Barale, J. F. R. Gower, & L. Alberotanza (Eds.), *Oceanography from Space* (pp. 273–287). Dordrecht: Springer Netherlands. doi:10.1007/978-90-481-8681-5

Castro, S. L., Wick, G. A., Minnett, P. J., Jessup, A. T., & Emery, W. J. (2010). The impact of measurement uncertainty and spatial variability on the accuracy of skin and subsurface regression-based sea surface temperature algorithms. *Remote Sensing of Environment*, *114*(11), 2666–2678. doi:10.1016/j.rse.2010.06.003

Chedin, A., Scott, N. A., & Berroir, A. (1982). A Single-Channel, Double-Viewing Angle Method for Sea Surface Temperature Determination from Coincident METEOSAT and TIROS-N Radiometric Measurements. *Journal of Applied Meteorology*, *21*(4), 613–618. doi:10.1175/1520-0450(1982)021<0613:ASCDVA>2.0.CO;2

Coats, R., Perez-Losada, J., Schladow, G., Richards, R., & Goldman, C. (2006). The Warming of Lake Tahoe. *Climatic Change*, *76*(1-2), 121–148. doi:10.1007/s10584-005-9006-1

Cornillon, P., Gilman, C., Stramma, L., & Brown, O. (1987). Processing and analysis of large volumes of satellite-derived thermal infrared data. *J. Geophys.*, *92*(7). Retrieved from http://po.gso.uri.edu/poweb/PCC/pcornillon/1987-Cornillonb.pdf

Cox, C., & Munk, W. (1954). Measurement of the roughness of the sea surface from photographs of the sun's glitter. *OURNAL OF THE OPTICAL SOCIETY OF AMERICA*, *44*(11), 838–850. Retrieved from http://userpages.umbc.edu/~martins/phys650/Cox and Munk Glint paper.pdf

Donlon, C. J., Minnett, P. J., Gentemann, C., Nightingale, T. J., Barton, I. J., Ward, B., & Murray, M. J. (2002a). Toward Improved Validation of Satellite Sea Surface Skin Temperature Measurements for Climate Research. *Journal of Climate*, *15*(4), 353–369. doi:10.1175/1520-0442(2002)015<0353:TIVOSS>2.0.CO;2

Donlon, C. J., Minnett, P. J., Gentemann, C., Nightingale, T. J., Barton, I. J., Ward, B., & Murray, M. J. (2002b). Toward Improved Validation of Satellite Sea Surface Skin Temperature Measurements for Climate Research. *Science And Technology*, *15*, 353–369.

Donlon, C. J., Rayner, N., Robinson, I., Poulter, D. J. S., Casey, K. S., Vazquez-Cuervo, J., Armstrong, E., et al. (2007). The Global Ocean Data Assimilation Experiment High-resolution Sea Surface Temperature Pilot Project. *Bulletin of the American Meteorological Society*, *88*(8), 1197–1213. doi:10.1175/BAMS-88-8-1197

Emery, W. J., Castro, S., Wick, G. A., Schluessel, P., & Donlon, C. (2001). Estimating Sea Surface Temperature from Infrared Satellite and In Situ Temperature Data. *Bulletin of the American*

Meteorological Society, *82*(12), 2773–2785. doi:10.1175/1520-0477(2001)082<2773:ESSTFI>2.3.CO;2

Emery, W. J., Fowler, C. W., Hawkins, J., & Preller, R. H. (1991). Fram Strait Satellite Image-Derived Ice Motions. *Journal of Geophysical Research*, *96*(C3), 4751–4768. doi:10.1029/90JC02273

Emili, E., Popp, C., Wunderle, S., Zebisch, M., & Petitta, M. (2011). Mapping particulate matter in alpine regions with satellite and ground-based measurements: An exploratory study for data assimilation. *Atmospheric Environment*, *45*(26), 4344–4353. doi:10.1016/j.atmosenv.2011.05.051

Etling, D. (2008). *Theoretische Meteorologie: eine Einführung* (3rd editio., p. 376). Berlin [and others]: Springer.

Friedman, D. (1969). Infrared Characteristics of Ocean Water (1 . 5-15 / i). *Applied Optics*, *8*(10), 2073–2078.

GCOS. (2006). *Systematic observation requirements for satellite-based products for climate - Supplemental details to the satellite-based component of the "Implementation Plan for the Global Observing System for Climate in Support of the UNFCCC." Organization* (Vol. 107, p. 235). Retrieved from http://www.wmo.int/pages/prog/gcos/Publications/gcos-107.pdf

Gentemann, C. L., Donlon, C. J., Stuart-Menteth, A., & Wentz, F. J. (2003). Diurnal signals in satellite sea surface temperature measurements. *Geophysical Research Letters*, *30*(3), 40_1 – 40_4. doi:10.1029/2002GL016291

Hale, G. M., & Querry, M. R. (1973). Optical Constants of Water in the 200-nm to 200-microm Wavelength Region. *Applied optics*, *12*(3), 555–63. Retrieved from http://www.ncbi.nlm.nih.gov/pubmed/20125343

Hampton, S. E., Izmest'Eva, L. R., Moore, M. V., Katz, S. L., Dennis, B., & Silow, E. a. (2008). Sixty years of environmental change in the world's largest freshwater lake - Lake Baikal, Siberia. *Global Change Biology*, *14*(8), 1947–1958. doi:10.1111/j.1365-2486.2008.01616.x

Hastings, D. A., & Emery, W. J. (1992). The advanced very high resolution radiometer (AVHRR): a brief reference guide. *Photogrammetric Engineering & Remote Sensing*, *58*(8), 1183–1188.

Hook, S. J., Chander, G., Barsi, J. A., Alley, R. E., Abtahi, A., Palluconi, F. D., Markham, B. L., et al. (2004). In-Flight Validation and Recovery of Water Surface Temperature With Landsat-5 Thermal Infrared Data Using an Automated High-Altitude Lake Validation Site at Lake Tahoe. *IEEE TRANSACTIONS ON GEOSCIENCE AND REMOTE SENSING*, *42*(12), 2767–2776.

Hook, S. J., Prata, F. J., Alley, R. E., Abtahi, A., Richards, R. C., Schladow, S. G., & Pálmarsson, S. Ó. (2003). Retrieval of Lake Bulk and Skin Temperatures Using Along-Track Scanning Radiometer (ATSR-2) Data : A Case Study Using Lake Tahoe , California. *Journal of Atmospheric and Oceanic Technology*, *20*, 534–548.

Hulley, G. C., Hook, S. J., & Schneider, P. (2011). Optimized split-window coefficients for deriving surface temperatures from inland water bodies. *Remote Sensing of Environment*, *115*(12), 3758–3769. doi:10.1016/j.rse.2011.09.014

Hüsler, F. (2012). *A satellite-based snow cover climatology derived from AVHRR data over the European Alps*. University of Bern.

Hüsler, F., Fontana, F., Neuhaus, C., Riffler, M., Musial, J., & Wunderle, S. (2011). AVHRR Archive and Processings Facility at the University of Bern: A comprehensive 1-km satellite dataset for climate change studies. *EARSEL Eproceedings*, *10*(2), 83–101.

ITT. (2009). What's New in IDL 7.1. ITT Visual Information Solutions.

Intergovernmental Panel on Climate Change (IPCC). (1990). Climate Change: The IPCC Scientific Assessment. Report prepared for Intergovernmental Panel on Climate Change by Working Group I. In J. T. Houghton, G. J. Jenkins, & J. J. Ephraums (Eds.), (p. 410 pp). Cambridge, Great Britain, New York, NY, USA and Melbourne, Australia: Cambridge University Press.

Intergovernmental Panel on Climate Change (IPCC). (1995). Climate Change 1995: The Science of Climate Change. Contribution of Working Group I to the Second Assessment Report of the Intergovernmental Panel on Climate Change. In J.T. Houghton, L. G. Meira Filho, B. A. Callander, N. Harris, A. Kattenberg, & K. Maskell (Eds.), (p. 584). Cambridge University Press, Cambridge, United Kingdom.

Intergovernmental Panel on Climate Change (IPCC). (2001). Climate Change 2001: The Scientific Basis. Contribution of Working Group I to the Third Assessment Report of the Intergovernmental Panel on Climate Change. In J T Houghton, Y. Ding, D. J. Griggs, M. Noguer, P. J. van der Linden, X. Dai, K. Maskell, et al. (Eds.), (p. 881). Cambridge University Press; Cambridge; United Kingdom and New York; NY; USA.

Intergovernmental Panel on Climate Change (IPCC). (2007). IPCC Fourth Assessment Report: Climate Change 2007. Contribution of Working Group I to the Fourth Assessment Report of the Intergovernmental Panel on Climate Change. In S. Solomon, D. Qin, M. Manning, Z. Chen, M. Marquis, K. B. Averyt, M. Tignor, et al. (Eds.), (p. 996). Cambridge University Press, Cambridge, United Kingdom and New York, NY, USA.

Jeffery, C., & Vazquez, J. (2011). *GHRSST - User Guide version 9* (p. 45).

Kaiser-Weiss, A., Minnett, P. J., Beggs, H., Armstrong, E., Casey, K., Merchant, C., Kaplan, A., et al. (2011). XII Science Team Meeting PROCEEDINGS OF THE GHRSST XII SCIENCE TEAM MEETING. *Proceedings of the GHRSSTXII Science Team Meeting* (p. 310).

Kilpatrick, K. A., Podestá, G. P., & Evans, R. (2001). Overview of the NOAA/NASA advanced very high resolution radiometer Pathfinder algorithm for sea surface temperature and associated matchup database. *J. Geophys. Res*, *106*(C5), 9179–9197. Retrieved from http://www.agu.org/journals/jc/jc0105/1999JC000065/pdf/1999JC000065.pdf

Kneizys, F. X., Abreu, L. W., Anderson, G. P., Chetwynd, J. H., Berk, A., & Way, V. (1996). *The MODTRAN 2/3 report and LOWTRAN 7 model*. *Contract* (pp. 508–689). Retrieved from http://www.gps.caltech.edu/~vijay/pdf/modrept.pdf

Kogan, F., Gitelson, A. A., Zakarin, E., Spivak, L., & Lebed, L. (2003). AVHRR-Based Spectral Vegetation Index for Quantitative Assessment of Vegetation State and Productivity: Calibration and Validation. *Photogrammetric Engineering & Remote Sensing*, *69*(8), 899–906.

Latifovic, R., & Pouliot, D. (2007). Analysis of climate change impacts on lake ice phenology in Canada using the historical satellite data record. *Remote Sensing of Environment*, *106*(4), 492–507. doi:10.1016/j.rse.2006.09.015

Li, X., Pichel, W., Clemente-Colón, P., Krasnopolsky, V., & Sapper, J. (2001). Validation of coastal sea and lake surface temperature measurements derived from NOAA/AVHRR data. *International Journal of Remote Sensing*, *22*(7), 1285–1303. doi:10.1080/01431160151144350

Liang, S. (2004). *Quantitative Remote Sensing of Land Surfaces*. (J. A. Kong, Ed.) (p. 534). Hoboken, New Jersey (USA): John Wiley & Sons, Inc.

Livingstone, D. M. (2003). Impact of Secular Climate Change on the Thermal Structure of a Large Temperate Central European Lake. *Climatic Change*, *57*(1/2), 205–225. doi:10.1023/A:1022119503144

Livingstone, D. M., & Lotter, A. (1998). The relationship between air and water temperatures in lakes of the Swiss Plateau: a case study with palaeolimnological implications. *Journal of Paleolimnology*, *19*, 181–198. Retrieved from http://www.springerlink.com/index/R15031255QH77X27.pdf

Llewellyn-Jones, D. T., Minnett, P. J., Saunders, R. W., & Zavody, A. M. (1984). Satellite multichannel infrared measurements of sea surface temperature of the N.E. Atlantic Ocean using AVHRR/2. *Quarterly Journal of the Royal Meteorological Society*, *110*(465), 613–631. doi:10.1002/qj.49711046504

MacCallum, P., & Merchant, C. (2011). *ATSR Reprocessing for Climate Lake Surface Water Temperature: ARC-Lake: Algorithm Theoretical Basis Document*. *October* (pp. 1–60). Retrieved from http://datashare.is.ed.ac.uk/bitstream/handle/10283/130/ARCLake_ATBD_v_1_1.pdf.txt

Martin, S. (2004). *An Introduction to Ocean Remote Sensing* (p. 454). Cambridge, UK: Cambridge University Press.

Masuda, K. (2006). Infrared sea surface emissivity including multiple reflection effect for isotropic Gaussian slope distribution model. *Remote Sensing of Environment*, *103*(4), 488–496. doi:10.1016/j.rse.2006.04.011

Masuda, K., Takashima, T., & Takayama, Y. (1988). Emissivity of pure and sea waters for the model sea surface in the infrared window regions. *Remote Sensing of Environment*, *24*(2), 313–329. doi:10.1016/0034-4257(88)90032-6

McClain, E. P., Pichel, W. G., & Walton, C. C. (1985). Comparative performance of AVHRR-based multichannel sea surface temperatures. *Journal of Geophysical Research*, *90*(C6), 11587–11601. Retrieved from http://www.agu.org/pubs/crossref/1985/JC090iC06p11587.shtml

McMillin, L. M. (1971). *A method of determining surface temperatures from measurements of spectral radiance at two wavelengths.* Iowa State University, Ames, USA.

McMillin, L. M. (1975). Estimation of sea surface temperatures from two infrared window measurements with different absorption. *Journal of Geophysical Research*, *80*(36), 5113–5117. Retrieved from http://www.agu.org/pubs/crossref/1975/JC080i036p05113.shtml

McMillin, L. M., & Crosby, D. S. (1984). Theory and validation of the multiple window sea surface temperature. *Journal of Geophysical Research*, *89*(4), 3655–3661. Retrieved from http://www.ocemwo.strony.univ.gda.pl/literatura/JC089iC03p03655.pdf

Merchant, C. J., Horrocks, L. A., Eyre, J. R., & O'Carroll, A. G. (2006). Retrievals of sea surface temperature from infrared imagery: origin and form of systematic errors. *Quarterly Journal of the Royal Meteorological Society*, *132*(617), 1205–1223. doi:10.1256/qj.05.143

Minnett, P. J., Smith, M., & Ward, B. (2011). Measurements of the oceanic thermal skin effect. *Deep Sea Research Part II: Topical Studies in Oceanography*, *58*(6), 861–868. doi:10.1016/j.dsr2.2010.10.024

OcCC. (2007). *Wasserwirtschaft. Klimaänderung und die Schweiz 2050 - Erwartete Auswirkungen auf Umwelt, Gesellschaft und Wirtschaft* (p. 172). Bern.

Oesch, D. C., Jaquet, J.-M., Hauser, A., & Wunderle, S. (2005). Lake surface water temperature retrieval using advanced very high resolution radiometer and Moderate Resolution Imaging Spectroradiometer data: Validation and feasibility study. *Journal of Geophysical Research*, *110*(C12), 1–17. doi:10.1029/2004JC002857

Oesch, D. C., Jaquet, J.-M., Klaus, R., & Schenker, P. (2008). Multi-scale thermal pattern monitoring of a large lake (Lake Geneva) using a multi-sensor approach. *International Journal of Remote Sensing*, *29*(20), 5785–5808. doi:10.1080/01431160802132786

O'Reilly, C. M., Alin, S. R., Plisnier, P.-D., Cohen, A. S., & McKee, B. a. (2003). Climate change decreases aquatic ecosystem productivity of Lake Tanganyika, Africa. *Nature*, *424*(6950), 766–8. doi:10.1038/nature01833

Peeters, F., Livingstone, D. M., Goudsmit, G.-H., Kipfer, R., & Forster, R. (2002). Modeling 50 years of historical temperature profiles in a large central European lake. *Limnology and Oceanography*, *47*(1), 186–197.

Persson, A. (2011). *Meteorological Bulletin M3.2: User guide to ECMWF forecast products* (p. 127). Retrieved from http://www.ecmwf.int/products/forecasts/guide/user_guide.pdf

Petty, G. W. (2006). *A first Course in Atmospheric Radiation* (Second Edi., p. 459). Madison, Wisconsin, USA: Sundog Publishing.

Petty, G. W. (2008). *A First Course in Atmospheric Thermodynamics* (1st editio., p. 338). Madison, Wisconsin, USA: Sundog Publishing.

Prabhakara, C., Dalu, G., & Kunde, V. G. (1974). Estimation of Sea Surface Temperature From Remote Sensing in the 11- to 13-µm Window Region. *Journal of Geophysical Research*, *79*(33), 5039–5044. doi:10.1029/JC079i033p05039

R Development Core Team. (2012). *R: A Language and Environment for Statistical Computing*. Vienna, Austria: R Foundation for Statistical Computing. Retrieved from http://www.r-project.org/

Riffler, M., Popp, C., Hauser, A., Fontana, F., & Wunderle, S. (2010). Validation of a modified AVHRR aerosol optical depth retrieval algorithm over Central Europe. *Atmospheric Measurement Techniques*, *3*(5), 1255–1270. doi:10.5194/amt-3-1255-2010

Robel, J. (2009). *NOAA KML User's Guide with NOAA-N,-P supplement*. Retrieved from http://www.ncdc.noaa.gov/oa/pod-guide/ncdc/docs/klm/index.htm

Rothman, L. S., Gordon, I. E., Barbe, A., Benner, D. C., Bernath, P. F., Birk, M., Boudon, V., et al. (2009). The HITRAN 2008 molecular spectroscopic database. *Journal of Quantitative Spectroscopy and Radiative Transfer*, *110*(9-10), 533–572. doi:10.1016/j.jqsrt.2009.02.013

Saunders, P. M. (1967). The temperature at the ocean-air interface. *Journal of the Atmospheric Sciences*, *24*, 269–273.

Saunders, P. M. (1968). Radiance of Sea and Sky in the Infrared Window 800-1200 cm^-1. *Journal of the Optical Society of America*, *58*(5), 645. doi:10.1364/JOSA.58.000645

Saunders, R. W., & Kriebel, K. T. (1988). An improved method for detecting clear sky and cloudy radiances from AVHRR data. *International Journal of Remote Sensing*, *9*(1), 123–150. doi:10.1080/01431168808954841

Schläpfer, D. (2011). *MODO User Manual, Version 5* (p. 96). Wil, Switzerland: ReSe Applications Schläpfer.

Schneider, P., & Hook, S. J. (2010). Space observations of inland water bodies show rapid surface warming since 1985. *Geophysical Research Letters*, *37*(22), 1–5. doi:10.1029/2010GL045059

Schneider, P., Hook, S. J., Radocinski, R. G., Corlett, G. K., Hulley, G. C., Schladow, S. G., & Steissberg, T. E. (2009). Satellite observations indicate rapid warming trend for lakes in California and Nevada. *Geophysical Research Letters*, *36*(22), 1–6. doi:10.1029/2009GL040846

Selby, J. E. A., & McClatchey, R. A. (1975). Atmospheric Transmittance From 0 . 25 t 28 . 5pMm : Computer Code LOWTRAN 3. *Environmental Research Papers*, *513*(May), 1–110.

Smith, L., Woolf, M., Abel, G., Hayden, M., Chalfant, M., & Groby, N. (1974). *NOAA Technichal Memorandum NESS 57 - NIMBUS-5 SOUNDER DATA PROCESSING SYSTEM. PART 1: Measurment Charateristics and Data Reduction Procedures (Final Report)* (p. 106). Washington, D.C (USA).

Sobrino, J. a., Raissouni, N., Simarro, J., Nerry, F., & Petitcolin, F. (1999). Atmospheric water vapor content over land surfaces derived from the AVHRR data: application to the Iberian Peninsula.

IEEE Transactions on Geoscience and Remote Sensing, *37*(3), 1425–1434. doi:10.1109/36.763306

Straile, D., Kerimoglu, O., Peeters, F., Jochimsen, M. C., Kümmerlin, R., Rinke, K., & Rothhaupt, K.-O. (2010). Effects of a half a millennium winter on a deep lake - a shape of things to come? *Global Change Biology*, *16*(10), 2844–2856. doi:10.1111/j.1365-2486.2009.02158.x

Takashima, T., & Takayama, Y. (1981). Emissivity and reflectance of the model sea surface for the use of AVHRR data of NOAA satellites. *Papers in Meteorology and Geophysics*, *32*(4), 267–274. doi:http://dx.doi.org/10.2467/mripapers.32.267

Tierney, J. E., Mayes, M. T., Meyer, N., Johnson, C., Swarzenski, P. W., Cohen, A. S., & Russell, J. M. (2010). Late-twentieth-century warming in Lake Tanganyika unprecedented since AD 500. *Nature Geoscience*, *3*(6), 422–425. doi:10.1038/ngeo865

Tomlinson, C. J., Chapman, L., Thornes, E., & Baker, C. (2011). Remote sensing land surface temperature for meteorology and climatology : a review. *Meteorological Applications*, *306*, 296–306. doi:10.1002/met.287

Trishchenko, A. P., Fedosejevs, G., Li, Z., & Zihlar, J. (2002). Trends and uncertainties in thermal calibration of AVHRR radiometers onboard NOAA-9 to NOAA-16. *Journal of Geophysical Research*, *107*(D24), 1–13. doi:10.1029/2002JD002353

Turner, J., & Warren, D. E. (1989). Cloud track winds in the polar regions from sequences of AVHRR images. *International Journal of Remote Sensing*, *10*(4-5), 695–703. doi:10.1080/01431168908903911

Verburg, P., & Hecky, R. E. (2009). The physics of the warming of Lake Tanganyika by climate change. *Limnology and Oceanography*, *54*(6, part 2), 2418–2430. Retrieved from http://www.aslo.orgwww.aslo.org/lo/toc/vol_54/issue_6_part_2/2418.pdf

Walton, C. C. (1988). nonlinear multichannel algorithm for estimating sea surface temperature with AVHRR satellite data.pdf. *Journal of Applied Meteorology*, *27*, 115–124.

Walton, C. C., Pichel, W. G., Sapper, J. F., & May, D. A. (1998). The development and operational application of nonlinear algorithms for the measurement of sea surface temperatures with the NOAA polar-orbiting environmental satellites. *Journal of Geophysical Research*, *103*(C12), 27999–28012. doi:10.1029/98JC02370

Wang, Y., Lean, J., & Sheeley Jr., N. (2005). Modeling the sun's magnetic field and irradiance since 1713. *The Astrophysical Journal*, *625*, 522–538. Retrieved from http://iopscience.iop.org/0004-637X/625/1/522

Watts, P. D., Allen, M. R., & Nightingale, T. J. (1996). Wind Speed Effects on Sea Surface Emission and Reflection for the Along Track Scanning Radiometer. *Journal of Atmospheric and Oceanic Technology*, *13*(1), 126–141. doi:10.1175/1520-0426(1996)013<0126:WSEOSS>2.0.CO;2

Wendisch, M., & Yang, P. (2012). *Theory of Atmospheric Radiative Transfer* (p. 321). Singapore: Wiley-VHC.

Wickham, H. (2009). *ggplot2 - Elegant graphics for data analysis*. New York: Springer. Retrieved from http://had.co.nz/ggplot2/book

Willmott, C. J., & Matsuura, K. (2005). Advantages of the mean absolute error (MAE) over the root mean square error (RMSE) in assessing average model performance. *Climate Research*, *30*, 79–82.

Wooster, M., Patterson, G., Loftie, R., & Sear, C. (2001). Derivation and validation of the seasonal thermal structure of Lake Malawi using multi-satellite AVHRR observations. *International Journal of Remote Sensing*, *22*(15), 2953–2972. doi:10.1080/01431160010006999

Wu, X., & Smith, W. L. (1997). Emissivity of rough sea surface for 8 - 13 um: modeling and verification. *Applied Optics*, *36*(12), 2609–2619.

Závody, A. M., Mutlow, C. T., & Llewellyn-Jones, D. T. (1995). A radiative transfer model for sea surface temperature retrieval for the along-track scanning radiometer. *Journal of Geophysical Research*, *100*(945), 937–952.

Appendix A

IDL Routines

The following list contains the names and short description of the main purpose of the IDL routines that have been developed during the course of the thesis:

Routine		**Purpose**
adapt_atm_profile.pro	-	IDL function that adapts the variables for the first ECMWF profile levels in order to match the atmospheric state actually present at the geographic location of the target pixel
cloud_corruption_filter.pro	-	IDL function that performs two simple cloud tests for the AVHRR observation provided with the calling sequence
compare_BTs.pro	-	IDL procedure for exporting coincident brightness temperatures from the RTTOV and MODTRAN IDL-save files
compute_sst.pro	-	IDL Function that computes the water-surface temperatures from an IDL save-file with AVHRR observations for a predefined period and a specified split-window-coefficients-file in the IDL-save format for a single pixel and performs some basic quality checks
compute_sst_bypatch.pro	-	Enhanced compute_sst.pro-IDL-Function that is able to compute mean water-surface temperature for a quadratic patch of a user-specified size around the target pixel (see compute_sst.pro for further details)

Routine		Purpose
import_avhrr_data.pro	-	IDL Function for importing AVHRR observations from the database into an IDL-save file for a predefined period
make_spectral_albedo_file.pro	-	IDL function that imports the emissivity as computed by Masuda (2006) via a bi-linear interpolation from the corresponding tables for AVHRR channels 3, 4 and 5
modtran_main.pro	-	IDL function that incorporates the entire processing chain included into the radiative transfer simulations starting from the cloud-testing, over the input-file generation, to the actual MODTRAN simulations (includes steps 1-7 in Figure 3)
nlsst_main.pro	-	IDL function that was intended to compute the split-window coefficients form the MODTRAN simulations, but was degraded to call the store_variabeles.pro for a user-specified period
read_atm_profile.pro	-	IDL function that imports the ECMWF profiles into variables
read_chn_file.pro	-	IDL function that imports the brightness temperatures from the MODTRAN chn-output-files
read_co2_data.pro	-	IDL function that imports the NOAA ESRL CO_2-tables obtained on Mouna Loa, Hawaii, USA
read_lakes_info.rpo	-	IDL function that reads and imports information for the target pixels, i.e. geographic location, elevation, ID
read_modtran_filename.pro	-	Function that reads and imports the systematically generated MODTRAN filenames into variables
read_spec_response.pro	-	Function that reads and imports the spectral response functions for the NOAA satellites
read_stations_info.pro	-	Function that reads and imports information for the target pixels, i.e. geographic location, elevation, unique lake-ID
read_tp5_file.pro	-	IDL function that reads the MODTRAN tp5-files and extracts the relative humidity, the wind speed, the total water vapor column and the total ozone column
read_tsi_data.pro	-	IDL function that imports the total solar irradiance table (i.e. the solar-constant) modeled by (Wang et al., 2005)
rescale_spec_resp.pro	-	IDL function for rescaling of NOAA satellite specific spectral response functions as provided by the NOAA KML User's guide

Routine		Purpose
run_all.pro	-	IDL procedure for running all, or particular main components of the algorithm consecutively and without interrupt
run_modo.pro	-	IDL function that starts the MODTRAN front-end MODO, and afterwards calls MODTRAN iteratively for the tp5-files that are existent in the user-specified input directory
splitwindow_coefficients.pro	-	IDL function that calculates split-window coefficients for a given period and a provided model output file. The function can handle RTTOV or MODTRAN outputs, dependent on the user-specified input parameters
spatial_comp.pro	-	IDL procedure that computes water-surface temperatures for two specific AVHRR scenes in April 2007. The function works very similar to the compute_sst_bypatch.pro function, but computes the water-surface temperatures for the entire AVHRR scene per provided set of split-window coefficients and computes the temperatures difference between both models, i.e. RTTOV minus MODTRAN
store_variables.pro	-	IDL function that collects the necessary parameters for the split-window coefficients computation from the MODTRAN output files for user-specified period. The functions stores the imported parameters combined into one IDL-save file.
time_shift_filter.pro	-	IDL function that removes entries an AVHRR ers-filename array and a corresponding AVHRR data-filename array in the common RSGB file-format, which are not within a user-specified window around 12 UTC
tp5_creator_lakes.pro	-	IDL function that generates the tp5-input files for MODTRAN radiative transfer simulations

The functions that are listed below comprise the unfinished and therefore not implemented water surface emissivity module after Masuda et al. (1988) and Masuda (2006):

Routine		**Purpose**
compute_p.pro	-	IDL function for computing the normalization factor p
compute_roh.pro	-	IDL function for computing the mean reflectivity rho from the facet
compute_sesr1.pro	-	IDL function for computing the 1st order surface-emitted surface-reflected emissivity
mean_emissivity.pro	-	IDL function that implements all other emissivity functions in order to obtain the mean emissivity from the facet, including the 1st order surface-emitted surface-reflected emission
read_refractive_index.pro	-	IDL function that reads the refractive index of water as computed by Hale & Querry (1973)
write_spec_alb_dat.pro	-	IDL function for writing the spectral albedo file in the appropriate MODTRAN file format

Appendix B

Complete overview of the in situ database

Lake	Elevation a.s.l. [m]	Latitude [°N]	Longitude [°E]	Reference Institution	Measurment period	Temporal resolution	Measurment depths [m]	Dataset ID
Lake Aegeri	7	47.123	8.618	AfU Zug	17.01.1990 - 15.11.2011	monthly	0 - 80	
Lake Baldegg	5	no information		UWE Luzern	09.01.1989 - 13.12.2010	monthly	0 - 65	
Lake Bienne	39	47.104	7.198	AWA Bern	28.02.1994 - 22.02.2012	monthly	0 - 10	
Lake Brienz	29	46.718	7.952	AWA Bern	15.02.1994 - 21.02.2012	monthly	0 - 10	
Lake Constance	541	47.624	9.375	LUBW	29.03.1989 - 27.06.2011	monthly	0 - 65	
Lake Constance	541	47.521	9.721	LUBW	10.01.1989 - 09.01.2012	monthly	0 - 250	
Lake Constance	541	47.720	8.986	LUBW	18.02.1997 - 10.01.2012	monthly	0 - 19	
Lake Constance	541	47.707	9.066	LUBW	03.01.1989 - 22.03.2011	monthly	0 - 46	
Lake Constance	541	47.676	9.001	LUBW	03.01.1989 - 10.01.2012	monthly	0 - 22	
Lake Constance	541	47.761	9.131	University of Konstanz	01.01.1987 - 20.03.2001	20 min*	0.1 - 9.6*	
Lake Constance	541	47.762	9.131	University of Konstanz	29.04.2004 - 20.08.2007	hourly	0.5 - 10.4	UniK
Lake Constance	541	47.507	9.748	Amt der Vorarlberger Landes-regierung	01.01.1997 - 12.31.2009	hourly	0 - 23	Brgz
Lake Geneva	583	46.453	6.589	CIPEL	16.01.1989 - 07.12.2010	monthly	0 - 10	
Lake Geneva	583	46.453	6.589	CIPEL	16.01.1989 - 08.12.2010	two weeks	0 - 10	
Lake Geneva	583	46.453	6.589	INRA	10.06.1991 - 31.10.2011	daily	0 - 1*	INRA

Lake	Elevation a.s.l. [m]	Latitude [°N]	Longitude [°E]	Reference Institution	Measurment period	Temporal resolution	Measurment depths [m]	Dataset ID
Lake Geneva	583	46.297	6.220	EPFL	03.02.2000 - 02.10.2011	hourly	1	EPFL[#]
Lake Lucerne	113	no information		UWE Luzern	01.02.1989 - 04.10.2010	quarterly	0 - 40	
Lake Neuchâtel	215	46.904	6.843	AfU Neuchâtel	27.06.2001 - 16.02.2012	monthly	0 - 10	
Lake Neuchâtel	215	46.909	6.845	DGT Neuchâtel	06.03.1989 - 16.11.2011	monthly	-	
Lake Morat	22	no information		AfU Fribourg	25.01.1989 - 11.10.2011	quarterly*	0 - 40	
Rotsee	0.5	no information		UWE Luzern	14.03.1989 - 02.11.2010	biannually	0 - 15	
Lake Sempach	14	no information		UWE Luzern	03.01.1989 - 06.12.2010	monthly	0 - 85	
Lake Thun	47	46.681	7.730	AWA Bern	02.03.1994 - 20.02.2012	monthly	0 - 10	
Lake Zug	38	47.101	8.493	AfU Zug	22.01.1990 - 20.12.2011	monthly	0 - 197	
Lake Zurich	88	47.312	8.569	University of Zürich	06.03.1989 - 16.03.2012	weekly*	0.05	

* Varying or inconsistent within the dataset.

[#] Data not shown. The ID could be encountered within the R and IDL source code.

Abbreviations

AfU	Amt für Umwelt, Switzerland
AWA	Amt für Wasser und Abfall, Switzerland
CIPEL	Commission internationale pour la protection des eaux du Léman, Switzerland
EPFL	École Polytechnique Fédérale de Lausanne, Switzerland
INRA	Institut national de la recherche agronomique, France
LUBW	Landesanstalt für Umwelt, Messungen und Naturschutz, Baden-Württemberg, Germany

Appendix C

Differences of model split-window coefficients

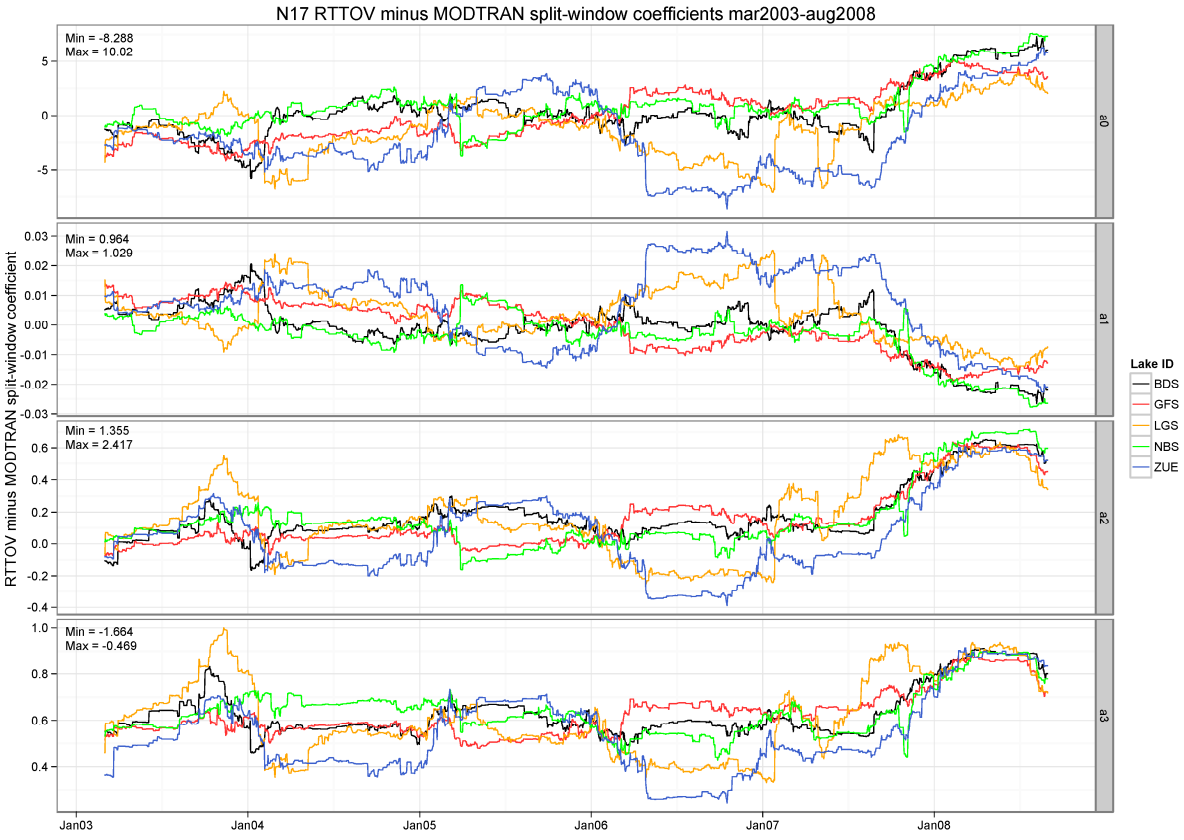

Figure 13: Model differences between the lake-specific split-window coefficients for NOAA 17 (N17) observations. Each panel refers to a different coefficient, which is indicated in the grey array on the right hand side of the panel. The coefficients a_0 to a_4 are denoted as in equation 4.1. Lake ID refer to Lake Constance (BDS, black), Lake Geneva (GFS, red), Lake Lugano (LGS, orange), Lake Neuchâtel (NBS, green) and Lake Zurich (ZUE, blue), respectively. As indication for the variability these differences represent when compared against the total variability of the corresponding coefficients, the minimum (Min) and the maximum (Max) are displayed in the upper left corner of each panel.

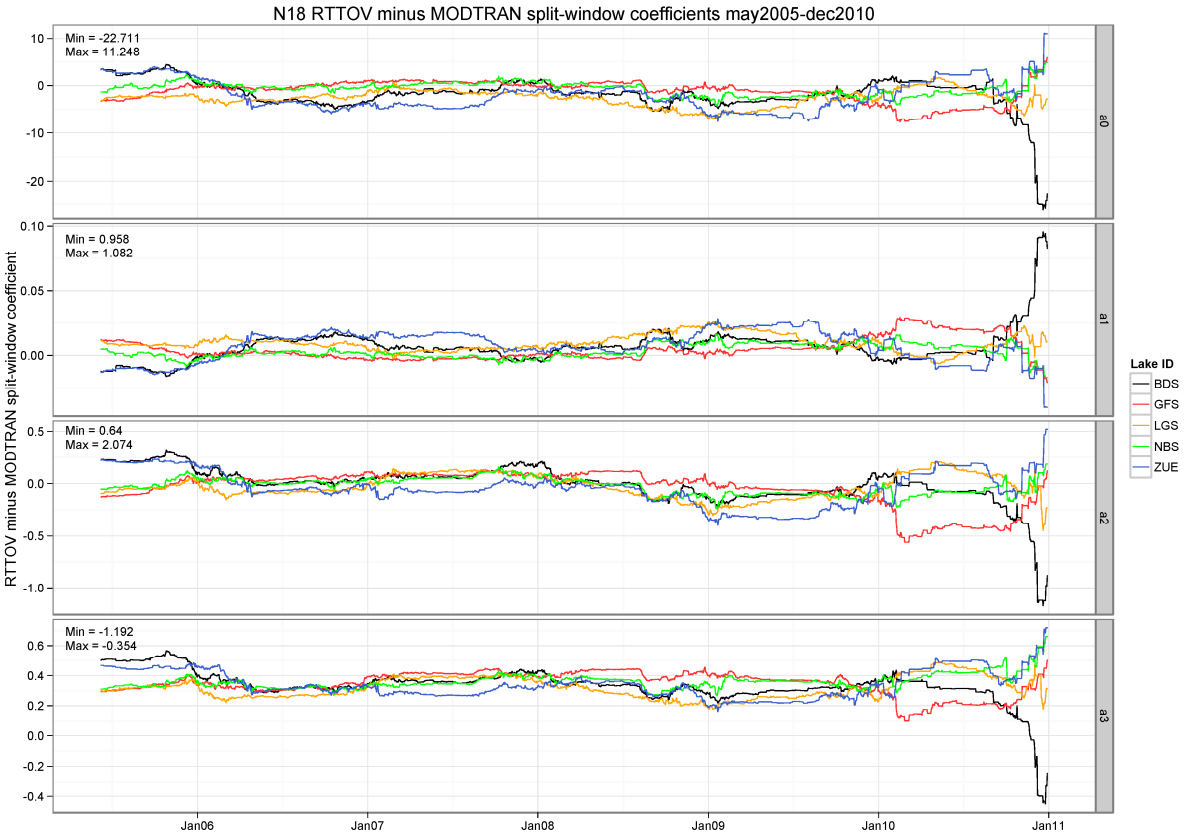

Figure 14: Model differences between the lake-specific split-window coefficients for NOAA18 (N18) observations. Each panel refers to a different coefficient, which is indicated in the grey array on the right hand side of the panel. The coefficients a_0 to a_4 are denoted as in equation 4.1. Lake ID refer to Lake Constance (BDS, black), Lake Geneva (GFS, red), Lake Lugano (LGS, orange), Lake Neuchâtel (NBS, green) and Lake Zurich (ZUE, blue), respectively. As indication for the variability these differences represent when compared against the total variability of the corresponding coefficients, the minimum (Min) and the maximum (Max) are displayed in the upper left corner of each panel.

Declaration

under Art. 28 Para. 2 RSL 05

Last, first name:	Sebastian Schulze
Matriculation number:	10-115-608
Programme:	Climate Sciences

Bachelor ☐ Master ☒ Dissertation ☐

Thesis title:	A comparison of MODTRAN and RTTOV radiative transfer models for lake surface water temperature retrieval
Thesis supervisor:	Dr. Stefan Wunderle

I hereby declare that this submission is my own work and that, to the best of my knowledge and belief, it contains no material previously published or written by another person, except where due acknowledgement has been made in the text. In accordance with academic rules and ethical conduct, I have fully cited and referenced all material and results that are not original to this work. I am well aware of the fact that, on the basis of Article 36 Paragraph 1 Letter o of the University Law of 5 September 1996, the Senate is entitled to deny the title awarded on the basis of this work if proven otherwise.

.....

Place, date

.....

Signature